

ABSTRACT

Title of Thesis: DURABILITY AND OPTIMIZATION
OF SOFC COMPOSITE CATHODES

Albert Painter, Masters of Science, 2016

Thesis Directed By: Professor Eric D. Wachsman, Materials Science
and Engineering

The combination of the conventional cathode material, $\text{La}_{0.8}\text{Sr}_{0.2}\text{MnO}_{3-\delta}$ (LSM), and exceptional oxygen ion conducting material, $(\text{Er}_{0.2}\text{Bi}_{0.8})_2\text{O}_3$ (ESB), has shown promise as a potential candidate for low temperature solid oxide fuel cell (LT-SOFC) cathodes. Though the initial performance of this composite is encouraging, the long-term stability of LSM-ESB has yet to be investigated. Here electrochemical impedance spectroscopy (EIS) was used to *in situ* monitor the durability of LSM-ESB at typical LT-SOFC operation temperatures. The degradation rate as a function of aging time was extracted based on the EIS data. Post analysis suggests that below 600 °C the order-disorder transition of ESB limits the performance due to a decrease in the oxygen incorporation rate. Above 600°C, the formation of secondary phases, identified as Mn-Bi-O, is the major performance degradation mechanism. Furthermore, the relative particle size of the LSM to ESB was optimized to minimize long-term degradation in cathode performance.

DURABILITY AND OPTIMIZATION OF SOFC COMPOSITE CATHODES

by

Albert Painter

Thesis submitted to the Faculty of the Graduate School of the
University of Maryland, College Park, in partial fulfillment
of the requirements for the degree of
Master of Science
2016

Advisory Committee:
Professor Eric D. Wachsman, Chair
Professor Isabel Lloyd
Professor Lourdes G. Salamanca-Riba

© Copyright by
Albert Painter
2016

Acknowledgements

I would like to first thank my advisor, Prof Wachsman, for his guidance throughout my graduate career and support for this work. As a dedicated proponent of energy research, Prof Wachsman has enabled myself and countless others to pursue our curiosities in this field.

I would also like to thank the many friends I have made in the Wachsman lab and throughout the University of Maryland. I would especially like to thank Yi-Lin Huang for his help in developing my research as well as his guidance while writing this thesis.

I also want to thank my parents, Steve and Loretta, my brother, Angelo, my girlfriend, Susannah, and her mother, Linda, for their endless encouragement.

This work was supported by National Energy Technology Laboratory (DE-FE0026189) as a subcontract to Redox Power Systems LLC.

Table of Contents

Acknowledgements.....	ii
Table of Contents	iii
List of Figures	iv
List of Abbreviations	vi
Chapter 1 : Introduction	1
1.1 Solid Oxide Fuel Cells	1
1.2 Cathode Contributions	4
1.3 Cell Construction and Materials Selection	6
1.4 Composite Cathode Durability	8
Chapter 2 : Theory and Experimental Setup.....	9
2.1 Electrochemical Impedance Spectroscopy	9
2.2 Symmetric Cell Preparation	12
2.3 Reactor Design.....	14
2.4 X-Ray Diffraction	15
2.5 Scanning Electron Microscopy	16
2.6 Laser Diffraction Particle Sizing	16
Chapter 3 : Long-Term LSM-ESB Aging	17
3.1 Introduction.....	17
3.2 Experimental	19
3.3 Results and Discussion	20
Chapter 4 : LSM-ESB Particle Size Optimization.....	33
4.1 Introduction.....	33
4.2 Experimental	33
4.3 Particle Size Analysis	34
4.4 Electrochemical Analysis.....	37
4.5 Conclusion	41
Chapter 5 : Future Work	43
5.1 Long-Term Aging	43
5.2 Particle Size Analysis	43
Bibliography	44

List of Figures

Figure 1.1.1: Theoretical fuel cell efficiencies with various fuels in comparison with Carnot efficiency with 25 °C exhaust temperature ¹	2
Figure 1.1.2: Diagram of SOFC components. O ₂ enters at the cathode and is reduced to O ²⁻ . The oxygen ions transport through the electrolyte and react with H ₂ to form H ₂ O ⁶	3
Figure 1.2.1: SOFC polarization losses as a function of current density ⁹	5
Figure 1.3.1: Structure of δ -Bi ₂ O ₃ with bismuth ions in red, oxygen ions in blue, and intrinsic oxygen vacancies in white ¹⁷	7
Figure 2.1.1: Typical Nyquist plot of cathode symmetric cell. Each decade is labeled (red). The total polarization and ohmic contribution shown.....	11
Figure 2.1.2: Typical equivalent circuit of electrochemical surface using the Voigt model. L is an inductor, R _{ohm} is the ohmic resistance, follow by two Voigt elements.	12
Figure 2.3.1: (Left) Image of single-cell reactor with symmetric cell sandwiched between Ag-wrapped alumina plates. (Right) Diagram of single-cell reactor. Gas flows through the inlet with the thermocouple and EIS leads and is exhausted through the outlet on the bottom.	14
Figure 2.3.2: Picture of four-cell reactor. A spring-loaded rod ensures that contact is maintained between the cell and current collectors during heating and cooling.	15
Figure 4.3.1: A) Powder XRD spectra of cpESB and ssESB milled for various durations. B) Close up of (200) ESB peak with full width at half maximum values and table of crystallite size calculated from the Scherrer equation.	35
Figure 4.3.2: SEM micrographs of cpESB powder and ssESB powders milled for various durations.	36
Figure 4.3.3: Laser scattering of cpESB powder and ssESB powders milled for various durations. Ethanol was used to disperse the particles. The table shows the average particle size of each sample. The samples highlighted in green were made into cathode paste.....	37
Figure 4.4.1: Nyquist plots of LSM-ESB symmetric cells aged at 650 °C. cpESB, ssESB milled for 4 h, 21 h and 310 h were used for the LSM-ESB composite cathode. The plots are shown for 0 h, 50 h, 100 h, and 150 h.....	38
Figure 4.4.2: A) Non-ohmic ASR of LSM-ESB symmetric cells aged at 650 °C fitted with linear trend lines. B) Time dependence of ohmic contribution of LSM-ESB symmetric cells aged at 650 °C.....	39
Figure 4.4.3: Degradation rate of non-ohmic ASR plotted against the ESB particle size. Dashed line show a potential exponential fit of data.	40
Figure 4.4.4: XRD spectra of freshly sintered LSM-ESB symmetric cells and LSM-ESB cells aged for 180 h at 650 °C. cpESB, ssESB milled for 4 h, 21 h and 310 h were used for the LSM-ESB composite cathode.	41

List of Abbreviations

SOFC: Solid Oxide Fuel Cell

LSM: $\text{La}_{0.8}\text{Sr}_{0.2}\text{MnO}_{3-\delta}$

ESB: $(\text{Er}_{0.2}\text{Bi}_{0.8})_2\text{O}_3$

ORR: Oxygen Reduction Reaction

YSZ: Ytria-Stabilized Zirconia

GDC: Gadolinium Doped Ceria

IT-SOFC: Intermediate Temperature SOFCs

LT-SOFC: Low Temperature SOFCs

OCV: Open Circuit Voltage

TPB: Triple Phase Boundary

ASR: Area Specific Resistance

EIS: Electrochemical Impedance Spectroscopy

CPE: Constant Phase Element

XRD: X-Ray Diffraction

SEM: Scanning Electron Microscopy

EDS: Energy Dispersive X-Ray Spectroscopy

TEM: Transmission Electron Microscope

FIB: Focused Ion Beam

cpESB: Coprecipitated ESB

ssESB: Solid State ESB

Chapter 1: Introduction

1.1 Solid Oxide Fuel Cells

In the undertaking to reduce reliance on fossil fuels and protect the environment solid oxide fuel cells (SOFCs) stand out as a promising solution^{1,2}. Fuel cells are energy conversion devices that directly oxidize fuel into electricity. Because they are not limited to the thermodynamic cycle of heat engines, the Carnot cycle, fuel cell's theoretical efficiency far exceeds conventional forms of energy generation. Figure 1.1.1 shows the theoretical efficiency of ideal fuel cells operating on various fuels in comparison to the Carnot efficiency of a heat engine. NO_x, SO_x, and CO₂ emissions are also much lower in fuel cells than heat engines. Unlike other fuel cells, SOFCs can utilize wide variety of fuels including hydrogen, natural gas and syngas. To accommodate these fuels SOFCs must run at much higher operating temperatures. However, this heat can be leveraged to further increase generation efficiency when used in combined heat and power applications³. Recent material breakthroughs in low temperature SOFCs have increased the thermodynamic efficiency as well as reduced the cost through inexpensive materials and shortened startup times^{4,5}.

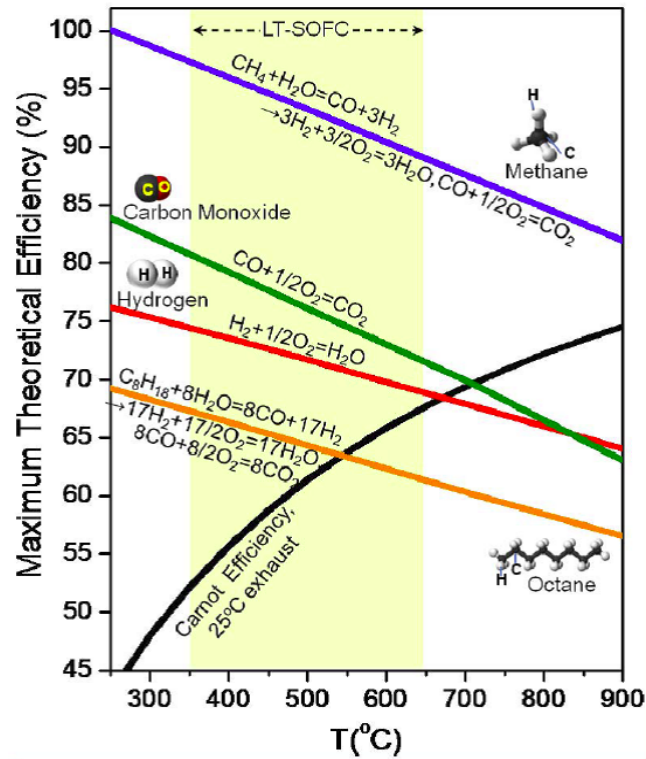
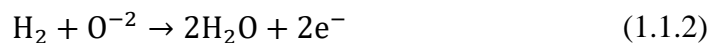


Figure 1.1.1: Theoretical fuel cell efficiencies with various fuels in comparison with Carnot efficiency with 25 °C exhaust temperature¹.

SOFCs consist of three active parts shown in Figure 1.1.2: the porous anode on the fuel side, followed by the dense, ion-conducting electrolyte, and porous cathode on the air side. The oxygen reduction reaction (ORR) is the process where oxygen molecules in the air are reduced to O^{2-} ions. The O^{2-} ions conduct through the solid state electrolyte into the anode where the O^{2-} ions oxidize the fuel. The ORR in the cathode is:



and, with H_2 gas as the fuel, the anode reaction is:



The overall reaction is:

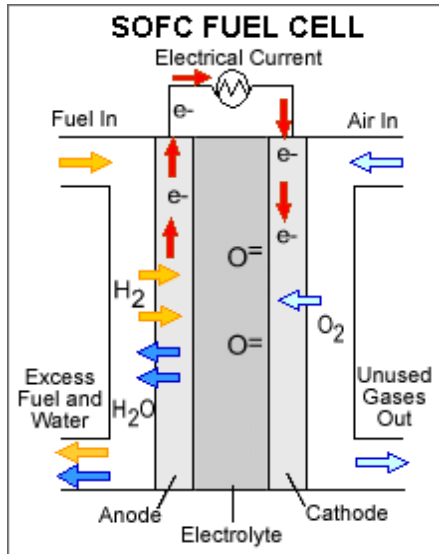


Figure 1.1.2: Diagram of SOFC components. O₂ enters at the cathode and is reduced to O²⁻. The oxygen ions transport through the electrolyte and react with H₂ to form H₂O⁶.

The conventional electrolyte material, yttria-stabilized zirconia (YSZ), has required SOFCs to operate at temperatures in excess of 1000 °C. Fortunately, new electrolyte materials like gadolinium doped ceria (GDC) and erbia-stabilized bismuth oxide (ESB) have opened up the possibility of lower operating temperatures⁷. Intermediate temperature SOFCs (IT-SOFCs) typically encompass temperatures from 650 °C to 800 °C. This range permits the use of more affordable materials as well as reduced startup times. Below 650 °C are the low temperature SOFCs (LT-SOFCs). LT-SOFCs further reduce cost as material compatibility increases with an exponential drop in insulation costs and degradation rates⁸.

1.2 Cathode Contributions

A useful measure of SOFC performance is the open circuit voltage (OCV), the voltage of the cell without current. The theoretical OCV can be calculated from the oxygen partial pressure using the Nernst equation:

$$\text{OCV} = \frac{RT}{4F} \ln \left(\frac{PO_2^{\text{fuel}}}{PO_2^{\text{air}}} \right) \quad (1.2.1)$$

where R is the gas constant, T is the absolute temperature, F is the Faraday constant, and PO_2 is the oxygen partial pressure of the fuel and air. However, actual fuel cells exhibit potentials lower than ideal due to three primary losses called polarizations: activation polarization, ohmic polarization and concentration polarization. The contribution of each of these polarizations as a function of current density is shown in Figure 1.2.1. Concentration polarization ($\eta_{\text{concentration}}$), sometimes called mass-transfer polarization, occurs when the supply of new reactants to the electrode is restricted due to limitations in gas diffusion. Ohmic polarization (η_{ohmic}) is primarily caused by the ionic resistance of the electrolyte. Activation polarization ($\eta_{\text{activation}}$) is due to the slow electrode kinetics and high reaction activation energy.

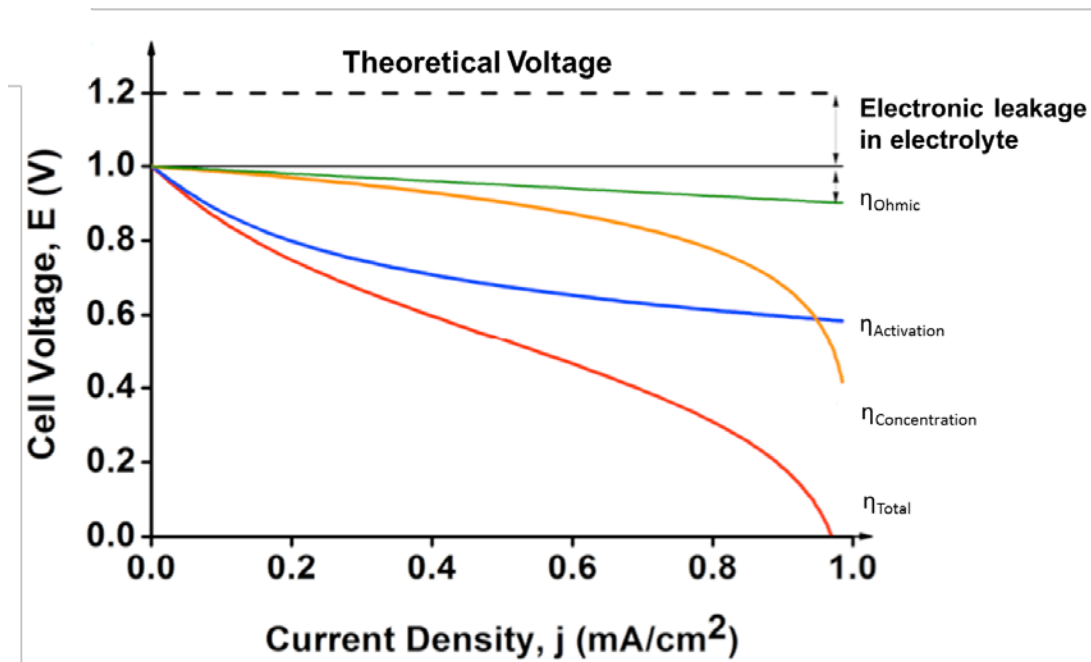


Figure 1.2.1: SOFC polarization losses as a function of current density⁹.

In SOFCs the dominating loss is from the activation polarization, specifically the ORR¹⁰. The ORR encompasses a complex set of processes including: oxygen adsorption, dissociation of the oxygen molecule, electrochemical charge transfer, surface diffusion, incorporation, and lattice diffusion¹¹. Furthermore, the cathode system under consideration determines the reaction steps and their contribution to the activation polarization. An important parameter in the study of SOFC cathodes is the triple phase boundary (TPB). Many cathode materials contain a two-phase mixture with an ionically-conducting phase and an electronically conducting phase. The meeting place of the two solid phases with the gaseous phase is the TPB. Because this interface is the meeting place of the oxygen gas, electrons, and oxygen ions, the geometry of the TPB plays a large role in the ORR.

1.3 Cell Construction and Materials Selection

Though GDC and ESB display high conductivity at low temperatures, certain obstacles prohibit their application in LT-SOFC electrolytes. GDC exhibits mixed ionic and electronic conductivity¹². Electronic conductivity in the electrolyte produces leakage current which further reduces the OCV of the cell. ESB, on the other hand, will reduce to Bi metal when subjected to the reducing conditions near the anode¹³. One solution to these challenges is to create a bilayer structure with a layer of GDC facing the anode and ESB facing the cathode^{14,15}. This accommodates both materials shortcomings. The ESB is protected from the reducing environment, and the leakage current from the GDC is blocked by the ESB layer. In addition to the electrolyte bilayer, a cell requires an anode and cathode. Ni-NiO cermet is a well-studied anode material suitable for this application. Though single-phase, mixed ionic and electronic cathodes exist, two-phase, composite cathodes benefit from longer TPBs and lower area specific resistance (ASR).

Of the oxygen ion conductors, cubic bismuth oxide, δ -Bi₂O₃, displays the highest O²⁻ conductivity. δ -Bi₂O₃ has a fluorite structure; however, due to the Bi³⁺ and O²⁻ stoichiometry, 25 % of the oxygen sites are left intrinsically vacant¹⁶⁻¹⁸. These vacancies, as seen in Figure 1.3.1, are the leading contributor to the materials conductivity. Unfortunately, many challenges have limited the widespread examination of δ -Bi₂O₃ in SOFC application. First, in reducing atmospheres, the δ -phase decomposes to bismuth metal, but this issue has been addressed in the previous section by implementing a bilayer electrolyte design. Second, the δ -phase becomes unstable at temperatures below ~750 °C¹⁹. After δ -Bi₂O₃ decays into a lower temperature phase, it

loses almost all of its ionic conductivity. A selection of lanthanide-based dopants have been shown to stabilize the δ -phase at low temperatures²⁰. The most conductive dopant composition, at least among the singly-doped δ - Bi_2O_3 , is $(\text{Er}_{0.2}\text{Bi}_{0.8})_2\text{O}_3$, where 20 % of the Bi sites are doped with Er²¹. Third, at temperatures below 650 °C, stabilized δ - Bi_2O_3 (i.e. ESB) undergoes an ordering process where oxygen vacancies align in the $\langle 111 \rangle$ direction^{22–25}. Following this order-disorder transition, the mobility of the oxygen vacancies drops and the ionic conductivity plummets.

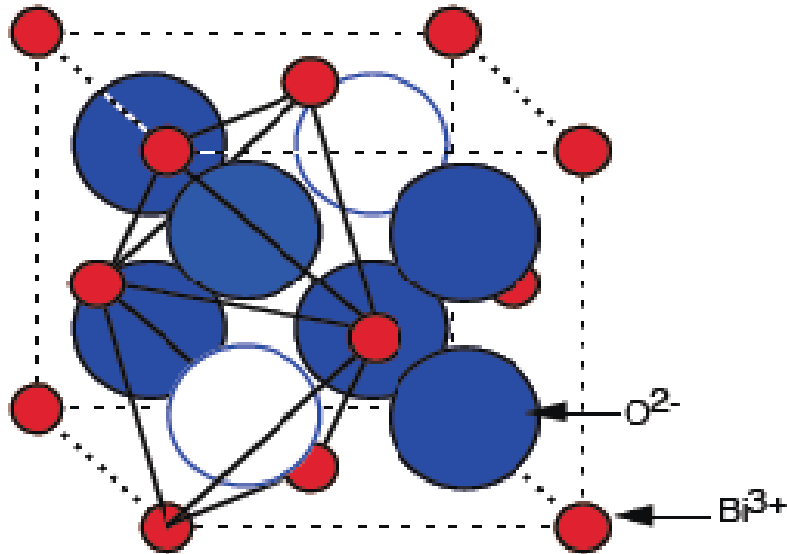


Figure 1.3.1: Structure of δ - Bi_2O_3 with bismuth ions in red, oxygen ions in blue, and intrinsic oxygen vacancies in white¹⁷.

The perovskite $(\text{La}_{0.8}\text{Sr}_{0.2})_{0.95}\text{MnO}_{3-\delta}$ (LSM) is one of the most well-studied cathode materials^{26,27}. The base material LaMnO_3 is a p-type conductor, but to further increase the conductivity, Sr is added to promote Mn^{4+} over Mn^{3+} and further boost the conductivity²⁸. Likewise, LSM is usually produced A-site deficient (lanthanum deficient) to repel the formation of secondary phases such as La_2O_3 . The thermal expansion and chemical stability of LSM makes it compatible with most SOFC

materials²⁹. In addition, LSM has high electronic conductivity and oxygen dissociation kinetics suitable for SOFC cathodes. Recently, LSM-ESB composite cathodes have been investigated and display considerable performance gains over LSM alone^{5,30}. This is especially the case when in contact with ESB electrolyte.

1.4 Composite Cathode Durability

In addition to the initial cathode performance the long-term durability of the cell is an important factor in the widespread adoption of SOFCs. Electrode degradation can be separated into reversible and irreversible processes. Reversible processes can be undone, often by performing a thermal treatment or flushing the electrode with a purifying gas. On the other hand, irreversible processes cannot be undone without reprocessing the electrode material. Degradation can further be divided into chemical and physical processes. Common chemical interactions include: secondary phase formation, interdiffusion, phase decomposition, and the order-disorder transition in ESB^{31,32}. In contrast, grain coarsening, delamination, and mechanical failures like cracking are possible forms of physical degradation^{10,33-35}. Although LSM-ESB has demonstrated great performance, the durability of the composite cathode has yet to be determined. The purpose of the study is to investigate the long-term performance and degradation mechanisms of LSM-ESB composite cathode for applications in a bilayer electrolyte SOFC.

Chapter 2: Theory and Experimental Setup

2.1 Electrochemical Impedance Spectroscopy

Electrochemical impedance spectroscopy (EIS) is a technique for measuring and separating processes in an electrochemical system³⁶. This is accomplished by measuring the impedance (Z) of a cell under an applied AC voltage. Impedance is a complex value where the resistance (Z') and reactance (Z'') are related by:

$$Z = Z' + jZ'' \quad (2.1.1)$$

The frequency of the applied voltage is then swept across a wide range. The resulting measurements are then formed into a Nyquist plot, sometimes called a complex plane plot, with Z' on the x-axis and $-Z''$ on the y-axis. An example Nyquist plot is shown in Figure 2.1.1. To extract information about the various electrochemical interfaces in the system, EIS spectra are fitted with equivalent circuits. A common approach to generating equivalent circuits is the Voigt model, whereby Voigt elements, a resistor and capacitor in parallel, are arranged in series to describe each electrochemical interface^{37,38}. The impedance of a Voigt element can be calculated by combining the impedance of a resistor and capacitor. The impedance of a resistor is:

$$Z_R = R \quad (2.1.2)$$

where R is the resistance of the resistor. The impedance of an ideal capacitor is:

$$Z_C = \frac{1}{j2\pi fC} \quad (2.1.3)$$

where f is the frequency of the AC voltage, and C is the capacitance. It follows that the impedance of the Voigt element is:

$$Z_{RC} = \frac{1}{\frac{1}{Z_R} + \frac{1}{Z_C}} = \frac{1}{R + j2\pi fC} \quad (2.1.4)$$

To better understand the ORR of a cathode, EIS is measured on cathode-electrolyte-cathode symmetric cells. By measuring a symmetric cell the effects of the cathode are isolated from the anode. The Nyquist plot of an actual cell has a few unique features. First, the high frequency intercept is off set from the origin in the direction of the real impedance. This resistance, R_{ohm} , preceding the Voigt elements relates to ohmic losses in the electrolyte and cathode. However, in cells with significantly thick electrolytes, the ohmic losses due to the cathode can be ignored. Second, there is a long tail leading up to the high frequency intercept. This inductor, L , is an artifact of the electrical test fixture. The equation for the impedance of an inductor is:

$$Z_L = j2\pi fL \quad (2.1.5)$$

where L is the inductance. The inductance, which appears as a vertical line in the Nyquist plot, is due to the inductance of the wires leading from the impedance analyzer to the cell as well as the electromagnetic field from heating elements in the furnace. Third, unlike an ideal Voigt element, the center point of the arc is not in the x-axis but, rather, below the axis. To better model the non-ideal nature of ORR processes, a constant phase element (CPE) is used in place of a capacitor in the Voigt element. The impedance of a CPE is:

$$Z_{CPE} = \frac{1}{(j2\pi f)^n Q} \quad (2.1.6)$$

where n is an empirical constant less than or equal to one, and Q is the capacitance. In the special case where n is unity, a CPE acts like an ideal capacitor. When the capacitor of the element is replaced with a CPE the impedance is:

$$Z_{RC} = \frac{1}{\frac{1}{R} + (j2\pi f)^n Q} \quad (2.1.7)$$

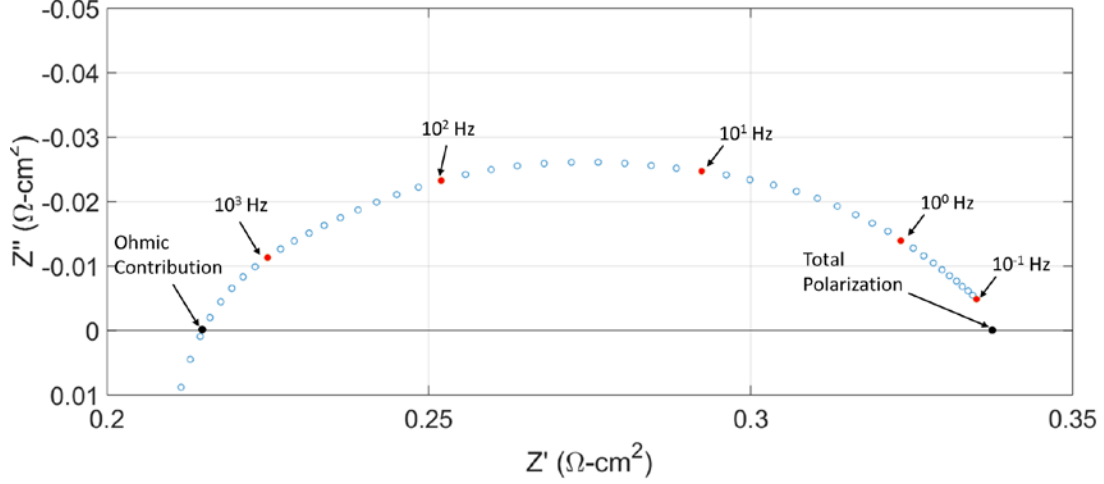


Figure 2.1.1: Typical Nyquist plot of cathode symmetric cell. Each decade is labeled (red). The total polarization and ohmic contribution shown.

If we interpret the above EIS spectrum as containing two semicircles inside the arc, the resulting equivalent circuit is shown in Figure 2.1.2. The impedance for this cell takes the form:

$$Z_{\text{cell}} = Z_L + Z_{\text{Rohm}} + Z_{\text{RC1}} + Z_{\text{RC2}} \quad (2.1.8)$$

or:

$$Z_{\text{cell}} = j2\pi fL + R_{\text{ohm}} + \frac{1}{\frac{1}{R_1} + (j2\pi f)^{n_1} Q_1} + \frac{1}{\frac{1}{R_2} + (j2\pi f)^{n_2} Q_2} \quad (2.1.9)$$

This model has eight independent variables which need to be fitted from the data: L , R_{ohm} , R_1 , n_1 , Q_1 , R_2 , n_2 , and Q_2 . In this study, MATLAB was used to optimize the variables. The conductivity of the electrolyte (σ) can be calculated by

$$\sigma = \frac{l}{R_{ohm}A} \quad (2.1.10)$$

here l is the thickness of the electrolyte and A is the cross sectional area of the electrolyte.

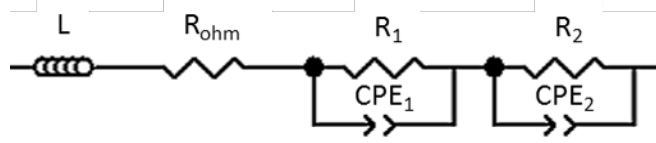


Figure 2.1.2: Typical equivalent circuit of electrochemical surface using the Voigt model. L is an inductor, R_{ohm} is the ohmic resistance, follow by two Voigt elements.

The non-ohmic polarization can be described by the resistance ($R_{cathode}$):

$$R_{cathode} = R_{tot} - R_{ohm} \quad (2.1.11)$$

where R_{tot} is the total resistance or the low frequency intercept. In the case of a cell with two semicircles:

$$R_{cathode} = R_1 + R_2 \quad (2.1.12)$$

$R_{cathode}$ measures the net effect of each ORR step. Polarizations are usually displayed as ASR:

$$ASR = \frac{R_{cathode}A}{2} \quad (2.1.13)$$

where A is the cross sectional area of the cathode. The factor of two accounts for the doubling of cathode polarizations in the symmetric cell configuration.

2.2 Symmetric Cell Preparation

Electrolyte pellets were made by uniaxially pressing 0.6 g of ESB powder (Trans-Tech) with a 1.0 cm die in a Carver benchtop press. The pellets were then sintered in air at 890 °C for 16 h. Following sintering the pellet diameter reduced to 0.805 cm and the

thickness to 0.141 cm. The faces of the pellets were then polished with 600 grit silicon carbide abrasive paper to prepare the surfaces for the cathode.

To create the LSM-ESB cathode, 0.9 g of ESB powder (Trans-Tech) was combined with 0.6 g of LSM powder (Fuel Cell Materials) to produce a 60:40 mass ratio of ESB:LSM or approximately 50:50 volume ratio of ESB:LSM. The mixture was ball milled in ethanol with 5 mm YSZ milling media for 24 h. A paste was created by slowly adding a Texanol-based vehicle (441 ESL Electroscience) while mixing in a THINKY ARE-310 planetary centrifugal mixer. Vehicle was added until the paste contained approximately equal mass of vehicle and LSM-ESB powder. Through mixing, ethanol was driven off to achieve a suitable consistency.

The cathode paste was applied to both sides of the electrolyte pellets via blade coating. Blade coating ensures a consistent, even cathode layer by drawing a rigid blade over a tape mask. The mask was created by layering two pieces of Scotch Magic tape and puncturing a 0.25 in (0.635 cm) diameter hole in the tape using a Neiko heavy duty hole punch. The mask was adhered to the face of the electrolyte pellet, and a small amount of cathode paste was applied to the surface. A razor blade was then wiped over the mask so the paste was even with surface of the mask. The mask was removed and the paste was dried in air at 120 °C for 20 minutes. This process was repeated for the opposite side of the pellet to create a symmetric cell. The cathode was sintered in a two-step process. First the cell was held at 400 °C for 2 h in air to burn off the vehicle from the paste. The temperature was then increased to 800 °C for 2 h in air to sinter the cathode to the electrolyte pellet. After sintering, Au paste (Heraeus) was painted on both faces of the symmetric cell to act as a current collector.

2.3 Reactor Design

Because the cell's electrochemical properties are heavily dependent on the testing atmosphere, a reactor setup is used to control the cell temperature and gas composition. Two homemade reactors were used to test the symmetric cells: a single-cell reactor and a four-cell reactor. Each reactor was placed in a tube furnace to regulate the temperature. An image and diagram of the single-cell reactor is shown in Figure 2.3.1. The single cell reactor uses a quartz closed-one-end tube to isolate the cell environment. The inlet gas, thermocouple, and EIS leads enter through the open end of the quartz tube. The open end is partially sealed to prevent backflow from ambient air. Ag mesh wrapped around two alumina plates acts as the current collector for the cell. The cell is clamped between the alumina plates by alumina nut and bolt sets. To reduce resistance and inductance from the leads, the single cell reactor uses four-point probe measurement where working and counter probes apply AC signal and primary and secondary reference probes collect the impedance.

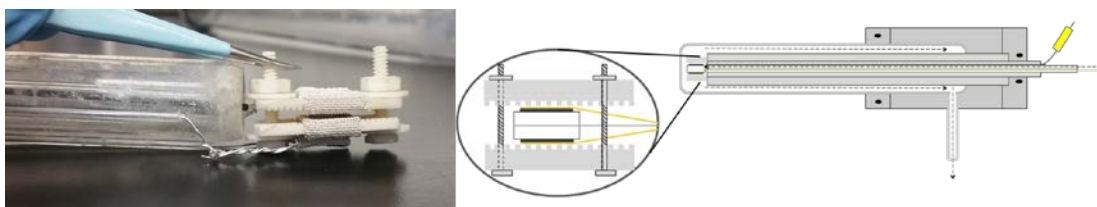


Figure 2.3.1: (Left) Image of single-cell reactor with symmetric cell sandwiched between Ag-wrapped alumina plates. (Right) Diagram of single-cell reactor. Gas flows through the inlet with the thermocouple and EIS leads and is exhausted through the outlet on the bottom.

The single cell reactor is sufficient for measuring single cell under different conditions; however, when multiple cells should be ran under the same conditions, it is preferred that the measurements be performed simultaneously in one reactor. A diagram of the four-cell reactor is shown in Figure 2.3.2. In order to accommodate four

cells an alumina open-both-ends tube encased the reactor. The inlet gas, thermocouple, and EIS leads enter through one end of the tube, and the gas is exhausted through a valve on the opposite end. To reduce the space needed to secure each cell, four spring-loaded tube and rod mechanisms clamped each of the cells between silver mesh current collectors. The four cell reactor was limited to two probe measurements for each cell.

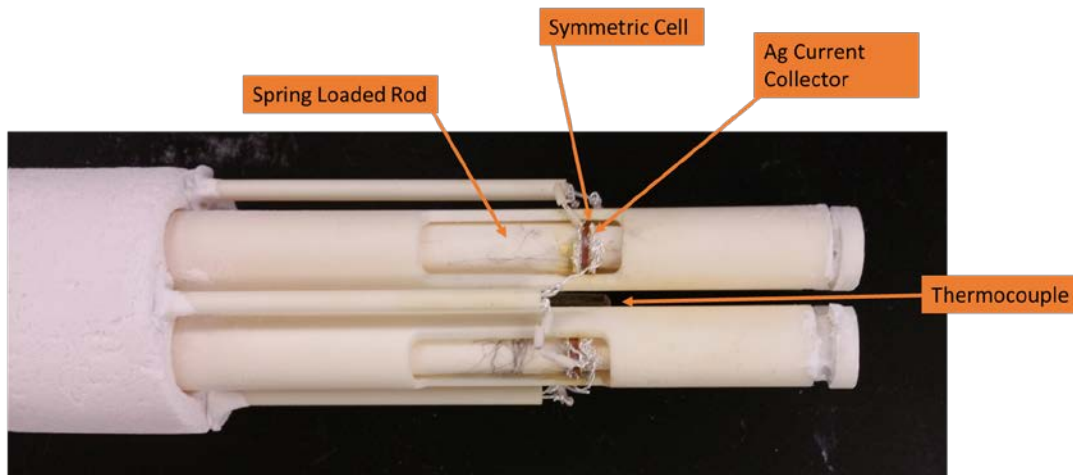


Figure 2.3.2: Picture of four-cell reactor. A spring-loaded rod ensures that contact is maintained between the cell and current collectors during heating and cooling.

2.4 X-Ray Diffraction

The phase purity of samples, both before and after aging, was determined by X-ray diffraction (XRD). For powder samples, the powder was lightly ground using a mortar and pestle. The powder was then mounted in quartz sample holders, and a glass slide was used to level the powder to the sample holder. For symmetric cell samples, the cells were mounted in clay and leveled with the samples holder. The XRD was performed with a Bruker D8 Advance using Cu $K\alpha$ radiation in the X-ray Crystallographic Center at the University of Maryland.

2.5 Scanning Electron Microscopy

Scanning electron microscopy (SEM) was used to characterize microstructure and morphology. A carbon-tape coated aluminum sample holder was used for all imaging. For powder samples, a small portion of powder was pressed onto the carbon tape. Excess powder was lightly blown off using compressed air. For pellet samples, the pellet was carefully fractured down the center. The pellet was then secured to the sample holder using additional carbon tape and the fractured surface facing the electron beam. To reduce charging, cross sectional samples were sputtered with gold. The Hitachi SU-70 FEG SEM in the University of Maryland NanoCenter AIMLab was used for all imaging.

2.6 Laser Diffraction Particle Sizing

The particle size and distribution of ESB powder was measured using laser diffraction particle size analysis. Samples were prepared by adding 0.01 g of ESB powder to 20 mL of ethanol. Each mixture was sonicated in an ultrasonic bath (Branson) for one hour in a glass vial. The HORIBA LA-960 Laser Particle Size Analyzer was used for all measurements. Before each measurement the cuvette was filled with ethanol, the analyzer was calibrated, and the 650 nm red laser and 405 nm blue LED were aligned. The ESB and ethanol solution was added with a micropipette until the solution came within optimal concentrations according to the analyzer software. A refractive index of 2.0 was used for all measurements.

Chapter 3: Long-Term LSM-ESB Aging

3.1 Introduction

Cubic bismuth oxide, $\delta\text{-Bi}_2\text{O}_3$, has attracted attention as a LT-SOFC electrolyte because it displays the highest O^{2-} conductivity of the low temperatures electrolytes^{16,17}. $\delta\text{-Bi}_2\text{O}_3$ has a fluorite structure, and due to the Bi^{3+} and O^{2-} stoichiometry 25 % of the oxygen sites are intrinsically vacant. These defects are responsible for the material's high ionic conductivity. To stabilize the δ -phase at temperatures lower than 730 °C, the Bi cation sites are often doped with lanthanides, with the highest single-dopant performance found when $\delta\text{-Bi}_2\text{O}_3$ is doped with 20 % Er_2O_3 ²¹. However, ESB exhibits a rapid decrease in ionic conductivity at temperatures below 600 °C, due to the order-disorder transition where the oxygen vacancies arrange in an ordered state at lower temperature. In the disordered state oxygen vacancies may occupy any of the eight oxygen sites in the fluorite lattice. In this state the oxygen vacancies are highly mobile leading to high overall ionic conductivity. However, below the order-disorder transition temperature, oxygen vacancies prefer to occupy sites in a $\langle 111 \rangle$ direction^{22,24}. The impact of the ordering on ionic conductivity, particularly for electrolyte applications, have been well studied, and many models have been proposed to describe the conductivity as a function of ordering fraction^{20,23}.

To leverage the high ionic conductivity in an LT-SOFC, ESB must be protected from the reducing environment of the anode. This has been accomplished through the use of the bilayer electrolyte design whereby a layer of GDC, an electrolyte with less conductivity but higher reducing stability than ESB, is used to separate the anode and

ESB layers. The bilayer electrolyte design offers a potential to increase the cell OCV and has demonstrated tremendous performance¹.

Due to the high reactivity of bismuth oxide, there is a lack of cathodes materials compatible with ESB electrolytes. Noble metals, including platinum and silver and conventional cathode materials, such as cobalt-based perovskites, have been shown to react with δ -Bi₂O₃^{39,40}. Bismuth ruthenate Bi₂Ru₂O₇ (BRO7) has been shown to be compatible with ESB as a BRO7-ESB composite cathode⁴¹. However, Kang Taek et al. reported that the composite cathode LSM-ESB demonstrates increased performance over BRO7-ESB with no secondary phase formation after sintering³⁰. In addition to bilayer electrolytes, LT-SOFC composite cathodes based on LSM and ESB have demonstrated significant performance gains over their single phase counterparts and make a promising candidate for bilayer electrolyte LT-SOFCs^{4,14,15,30}. ESB's high ionic conductivity in combination LSM's high electronic conductivity and high oxygen dissociation kinetics provide a low ASR cathode³⁰. Although LSM-ESB has shown good initial performance as an LT-SOFC cathode, the long-term durability of these materials in LT-SOFC conditions has not yet been determined. Also, there has been little investigation of the link between cathode performance and the ESB order-disorder transition. To bring SOFCs to commercial fruition, it is essential to consider the stability of the system. A more fundamental understanding of these degradation mechanism can further aid in the selection of materials and the development of new designs.

In this study we investigate the durability of LSM-ESB symmetric cells in the LT-SOFC temperature range (500-650 °C). During aging electrochemical impedance

spectroscopy (EIS) was used to monitor the change in cathode ASR. Post-analysis techniques were applied to aged samples to identify the changes in microstructure and phase purity. Based on the results of time dependent EIS spectra and the post-characterization results, we can propose the possible degradation mechanisms for LSM-ESB composite cathodes.

3.2 Experimental

Electrolyte pellets for symmetric cells were prepared by uniaxially pressing ESB powder (Trans-Tech) and sintering the pellets at 890 °C for 16 h in air. Cathode paste was created by combining ESB powder (Trans-Tech) and LSM powder (Fuel Cell Materials) in a 60:40 (ESB:LSM) mass ratio with A Texanol-based vehicle (441 ESL Electrosience). To obtain uniform cathode thickness between cells the LSM-ESB paste was blade-coated on both sides of the ESB electrolyte. The cathode was sintered in a two-step process. First the cell was held at 400 °C for 2 h in air to burn off the vehicle from the paste. The temperature was then increased to 800 °C for 2 h in air to sinter the cathode to the electrolyte pellet.

The details in the experimental setup for EIS measurement can be found in our previous work³¹. A custom built reactor is used for EIS (Solartron 1470E) testing. Samples were clamped in two alumina plates using alumina bolts to ensure good contact between cathodes and current collectors. Synthetic air (AIRGAS) is flowed into the reactor at a rate of 100 SCCM. A four-wire, two-point measurement was used with a 20 mV AC signal applied from 10 kHz to 10 mHz or 1 mHz in an open-circuit configuration. A homemade MATLAB script was used to separate the ohmic and non-

ohmic polarization of each EIS measurement and determine the ASR as a function of time.

SEM was used to characterize the cathode microstructure. XRD was performed on the surfaces of fresh and aged cells to determine phase purity and identify secondary phases formed during aging. Samples were prepared for energy dispersive x-ray spectroscopy (EDS), electron energy loss spectroscopy (EELS) and transmission electron microscopy (TEM, JEOL JEM 2100 LaB6) by focused ion beam (FIB)/SEM (Tescan XEIA Plasma) milling to create a thin cathode cross sections.

3.3 Results and Discussion

To better understand the effects of the order-disorder transition on the performance of LSM-ESB composite cathode, four symmetric cells were aged at 500, 550, 600, and 650 °C for approximately 180 h while EIS measurements were taken every hour. The Nyquist plots of each aged cell are shown in Figure 3.3.1. From these spectra the ohmic (ASR_{ohmic}) and non-ohmic ($ASR_{non-ohmic}$) contribution to the symmetric cell were extracted. It is apparent that the 500 °C and 550 °C undergo significant degradation in non-ohmic polarization, at 500 °C between 0 h and 50 h and at 500 °C between 50 h and 100 h. The time dependent changes in ASR_{ohmic} fit the characteristic shapes of ordering in ESB. Since the high frequency intercept of the spectra changed dramatically due to the ordering of the ESB, the arcs were ohmic corrected to directly compare the changes of non-ohmic ASR as a function of aging time. The initial $ASR_{cathode}$ of the LSM-ESB cathodes at 500, 550, 600 and 650 °C was 3.43, 1.02, 0.38, and 0.12 $\Omega\text{-cm}^2$. This performance is comparable to the previous investigation of LSM-ESB electrode on ESB electrolyte³⁰.

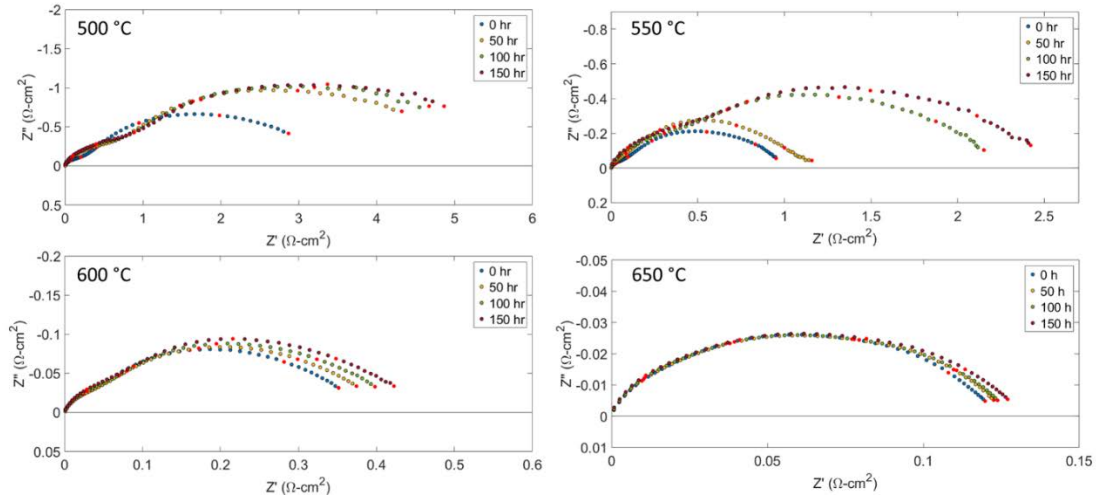


Figure 3.3.1: Ohmic-corrected Nyquist plots of LSM-ESB symmetric cells aged at 500 °C, 550 °C, 600 °C, and 650 °C shown at aging time 0 h, 50 h, 100 h, and 150 h.

The total ASR of the cells as a function of aging time is plotted in Figure 3.3.2a.

The relative ohmic ASR and reciprocal ohmic ASR deconvoluted from EIS spectra are shown in Figure 3.3.2b and Figure 3.3.2c, respectively. To confirm that the changes in ohmic ASR are due to anion ordering of ESB, the relative conductivity of ordering ESB from literature is shown in Figure 3.3.2d⁴². The ESB conductivity and reciprocal ohmic ASR share similar features below the order-disorder temperature. The greatest drop in conductivity occurs when aging at 550 °C. Also at 550 °C, the plots display the characteristic “S” shaped profile with a delayed drop in conductivity. Similarly, aging at 500 °C has a less dramatic drop to conductivity but with immediate impacts upon aging. By this comparison, it appears that the increase in relative ohmic ASR is a product of ESB anion ordering. Likewise, at 650 °C, above the order-disorder transition temperature, there are no signs of ordering. The relative non-ohmic ASR and reciprocal non-ohmic ASR extracted from the EIS are shown in Figure 3.3.2e and Figure 3.3.2f, respectively. When compared to the ohmic ASR, the non-ohmic ASR clearly show signs of ordering at between 500 °C and 600 °C. This degradation profile indicates that

the ordering of ESB oxygen vacancies not only impacts ESB's ionic conductivity, but also the ORR of the LSM-ESB composite. Specifically, the ordered ESB inhibits the oxygen incorporation step of the ORR and increases the ASR of the cathode.

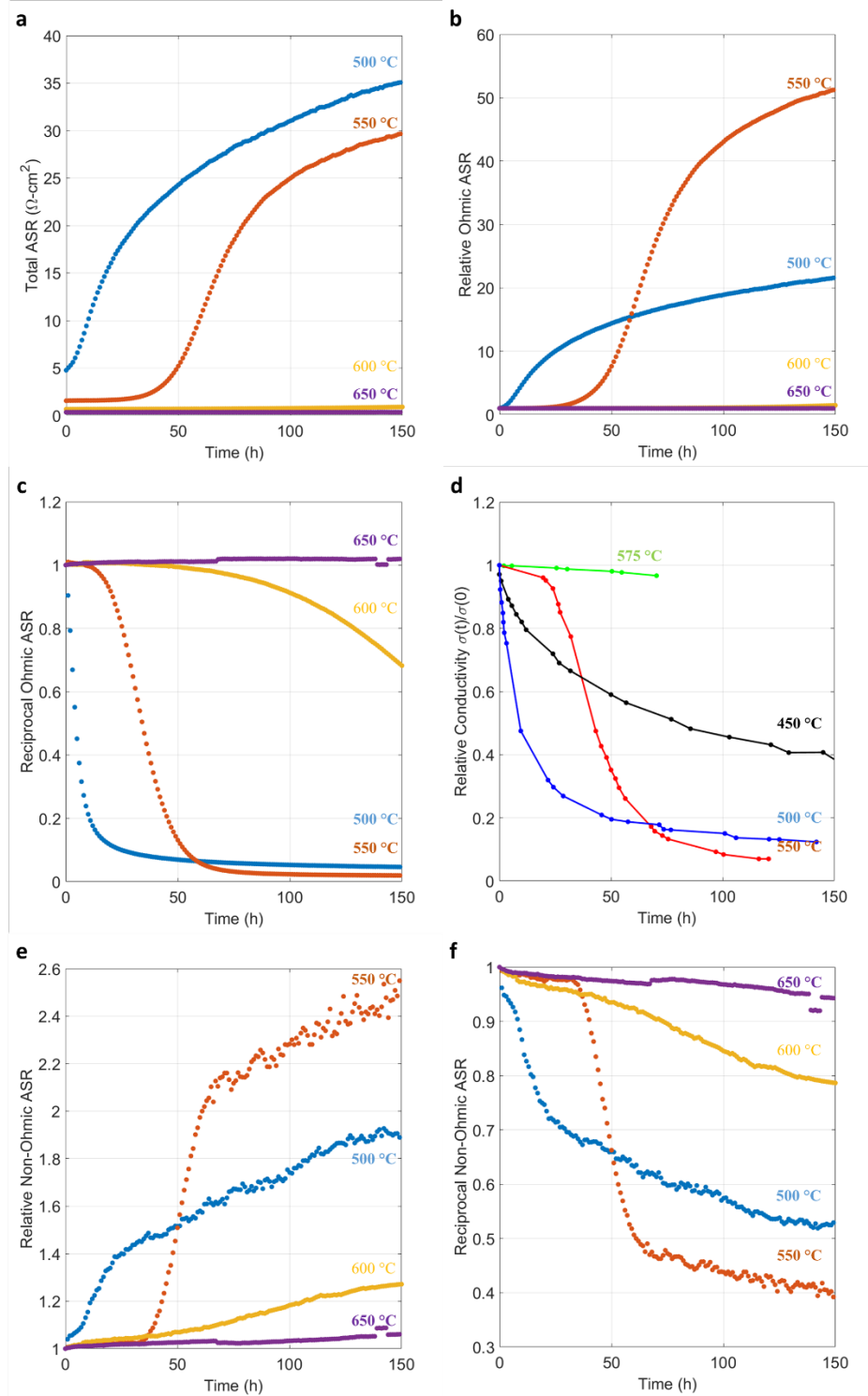


Figure 3.3.2: (a) total ASR over aging time of LSM-ESB symmetric cells aged at 500, 550, 600, and 650 °C, (b) ohmic ASR normalized to the initial ohmic ASR, (c) reciprocal of the ohmic ASR, (d) conductivity of ESB during ordering⁴², (e) non-ohmic ASR normalized to the initial ohmic ASR, (f) reciprocal of the non-ohmic ASR.

The XRD spectra of each of the aged cells along with a freshly sintered cell is shown in Figure 3.3.3. Due to remnants from current collector, Metallic Au peaks are present in the aged samples. The freshly sintered sample displays no observable secondary phase formation brought on by the sintering process. Similar, the cells aged for 180 h from 500 °C to 600 °C maintained distinct LSM and ESB spectra with no secondary phase formation. The spectrum of the cell aged at 650 °C shows the possible formation of secondary phases; however, aging for 180 h does not yield sufficient peak intensity to identify the phases.

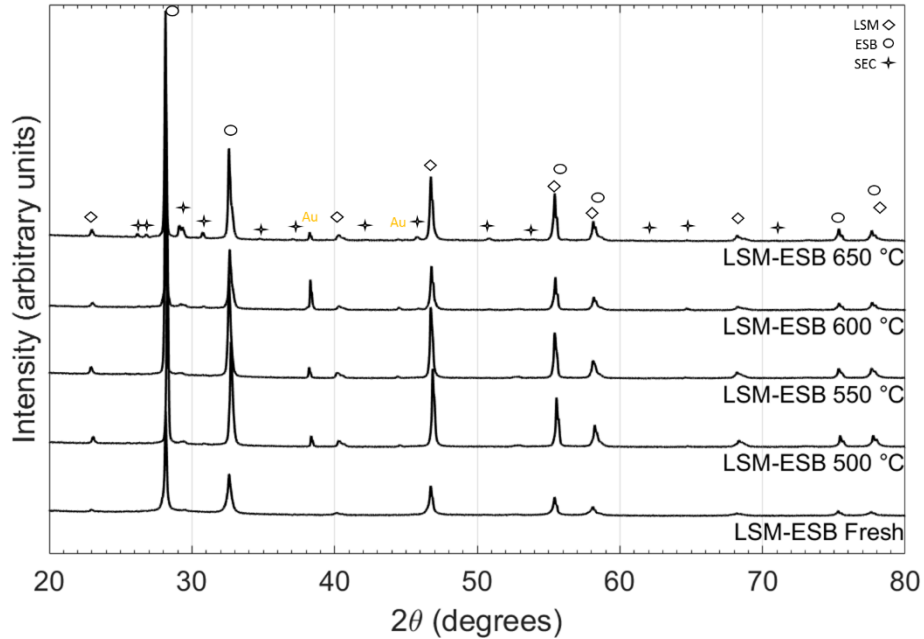


Figure 3.3.3: XRD spectra of freshly sintered LSM-ESB symmetric cell and LSM-ESB cell aged for 180 h at 500 °C, 550 °C, 600 °C, and 650 °C.

To increase the intensity of secondary phase formation and determine additional possible degradation mechanisms without the effects of ESB ordering, an LSM-ESB symmetric cell was aged at 650 °C for 500 h in synthetic air. The ohmic corrected impedance spectra of the cell at time 0 h, 250 h and 500 h is shown in Figure 3.3.4a.

Figure 3.3.4b shows the relative change in ohmic and non-ohmic ASR as a function of time. The initial ohmic and non-ohmic ASR is $0.21 \text{ } \Omega\text{-cm}^2$ and $0.13 \text{ } \Omega\text{-cm}^2$, respectively. A linear fit of the slope of ASR is used to extract the degradation rate. The non-ohmic ASR increases at a rate of 5.8 % per 100h. In comparison, there is no change in the ohmic ASR over the course of the aging, suggesting the conductivity of the ESB electrolyte is not affected during aging at 650 °C. The $\log(\text{ASR})$ as a function of reciprocal temperature is shown in Figure 3.3.5. The Arrhenius relationship was used to calculate apparent activation energy, E_A , of the cathode. The shift of the curve confirms that the cathode performance decreases after aging. The activation energy of the LSM-ESB decreased slightly from 1.18 eV to 1.09 eV after aging. This small decrease in E_A after aging suggest that LSM-ESB aged at 650C for 500 hours may have minimal impact on the ORR pathway of LSM-ESB.

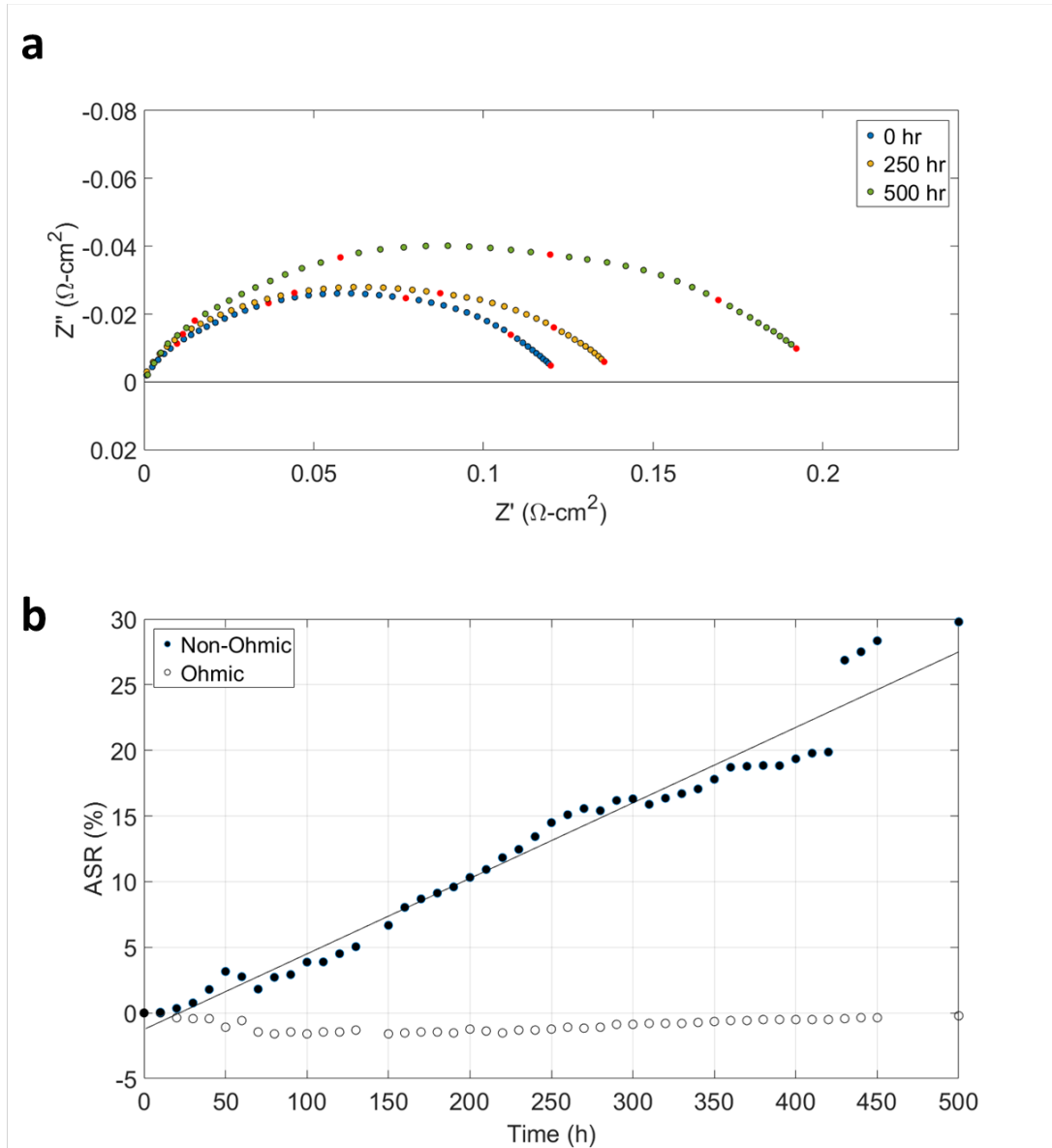


Figure 3.3.4: (a) Ohmic-corrected Nyquist plot of LSM-ESB symmetric cell at 650 °C at 0 h, 250 h and 500 h and (b) ohmic and non-ohmic ASR as a percentage change from the initial performance. The open circles represent the ohmic contribution and closed circles represent the non-ohmic contribution.

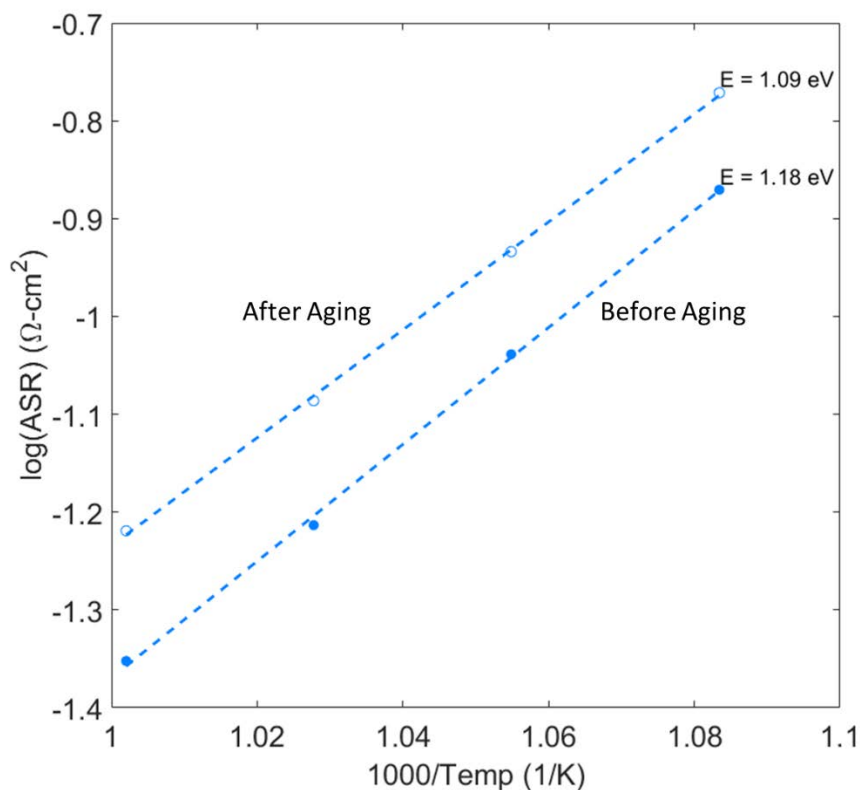


Figure 3.3.5: The log of the non-ohmic ASR a function of inverse temperature for LSM-ESB symmetric cell before and after aging at 650 °C for 500 h.

To determine the microstructure of the porous electrode, the cross-sectional backscatter SEM micrographs of the freshly sintered and aged LSM-ESB cathodes are shown in Figure 3.3.6a. Due to the higher atomic number of bismuth, the bismuth-containing phases have a higher intensity and appear brighter in the backscatter images than the LSM particles. In general, the LSM and ESB phases appear to be well distributed throughout the electrode. To quantitatively analyze the microstructure, a particle size analysis was performed using MATLAB to separate the LSM and ESB phases by their intensity and determine the average particle size. Figure 3.3.6b shows the phase separation of phases before and after aging with the ESB phases outlined in green and the LSM phases outlined in red. The average phase area was determined for

each particle and the circle-equivalent particle diameter was calculated for each phases. Over the course of aging, the circle-equivalent particle diameter of the ESB and LSM changed from 266 nm to 436 nm and 327 nm to 300 nm, respectively. The LSM particles had a small reduction in size but remained nearly the same. In contrast, the average ESB particle size increased by ~60 %. This may be a result of bismuth's volatility at high temperatures⁴³. This indicates that grain coarsening of the ESB phase may be a potential degradation mechanism of the LSM-ESB cathode.

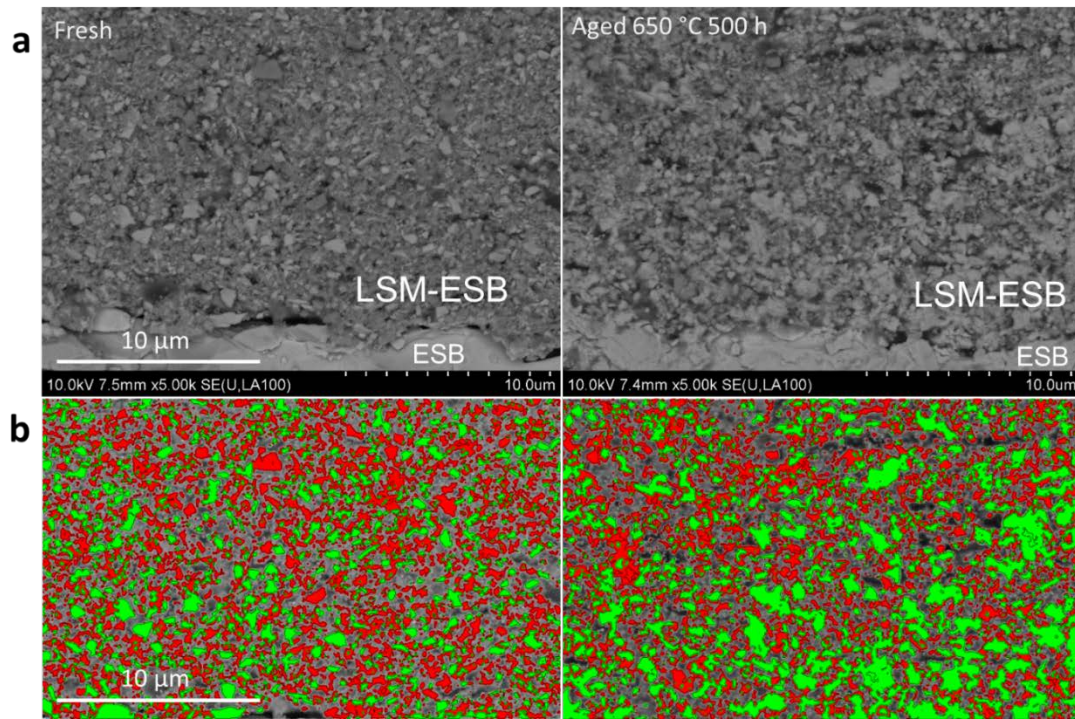


Figure 3.3.6: (a) SEM micrographs of LSM-ESB symmetric cell cross section (left) freshly sintered cell and (right) cell aged at 650 °C for 500 h and (b) segmented images of (left) freshly sintered cell and (right) cell aged at 650 °C for 500 h with ESB particle outlined in green and LSM particles outlined in red.

Another possible degradation mechanism is the formation of secondary phases. XRD spectra of the sample before and after aging are shown in Figure 3.3.7. Again, the spectrum of the fresh cell indicates that there are no reactions between and LSM and ESB phases during the cathode sintering process. After aging at 650 °C for 500 h

the XRD spectrum shows the formation of secondary phases, possibly $\text{Bi}_8\text{La}_{10}\text{O}_{27}$ and BiMn_2O_5 . This indicates that reactions between bismuth and the LSM cathode components produce secondary phases as a degradation mechanism.

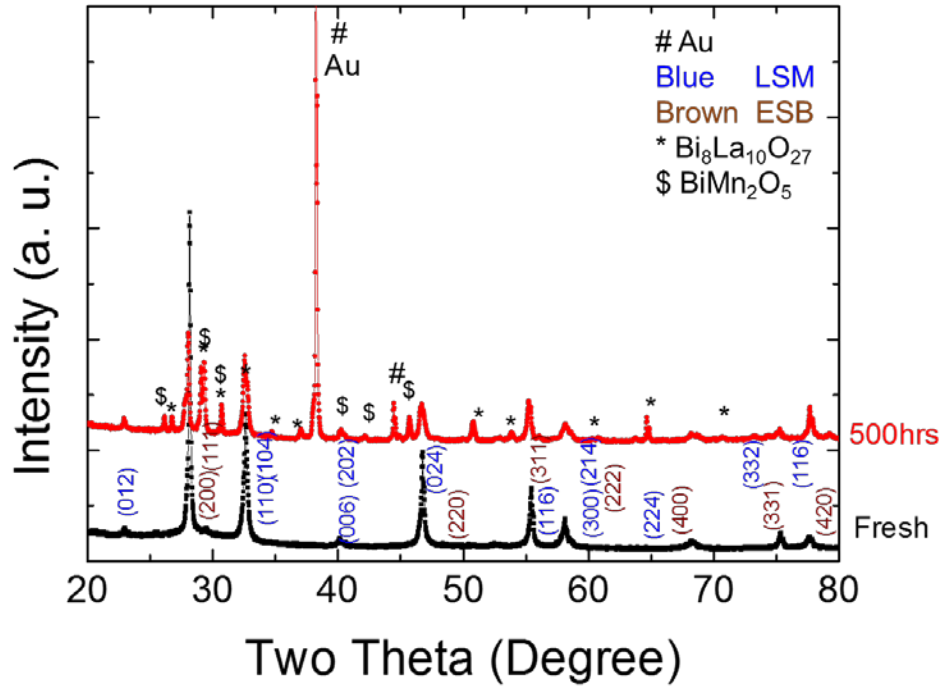


Figure 3.3.7: XRD spectra of freshly sintered LSM-ESB symmetric cell (black) and LSM-ESB cell aged for 500 h at 650 °C (red).

In order to identify the composition of these secondary phases and further characterize the cathode microstructure, the aged cell was analyzed using EDS for TEM. The TEM micrograph, EDS mapping, and EDS point analysis in Figure 3.3.8 shows the presence of a BiMn_2O_5 particle. The EDS point analysis reveals a 2 to 1 ratio of Mn to Bi which is consistent with the BiMn_2O_5 structure identified by the XRD. In addition, bismuth containing nanoparticles were found on the porous electrode surface. These nanoparticles, shown in Figure 3.3.9, could be to the precipitation of bismuth on the LSM surface at high temperatures. Thus a potential mechanism for the formation

of Bi-Mn-O phases is the precipitation of bismuth onto the LSM surface followed by reaction between the bismuth and manganese. TEM analysis was unable to identify the occurrence of any $\text{Bi}_8\text{La}_{10}\text{O}_{27}$ secondary phase.

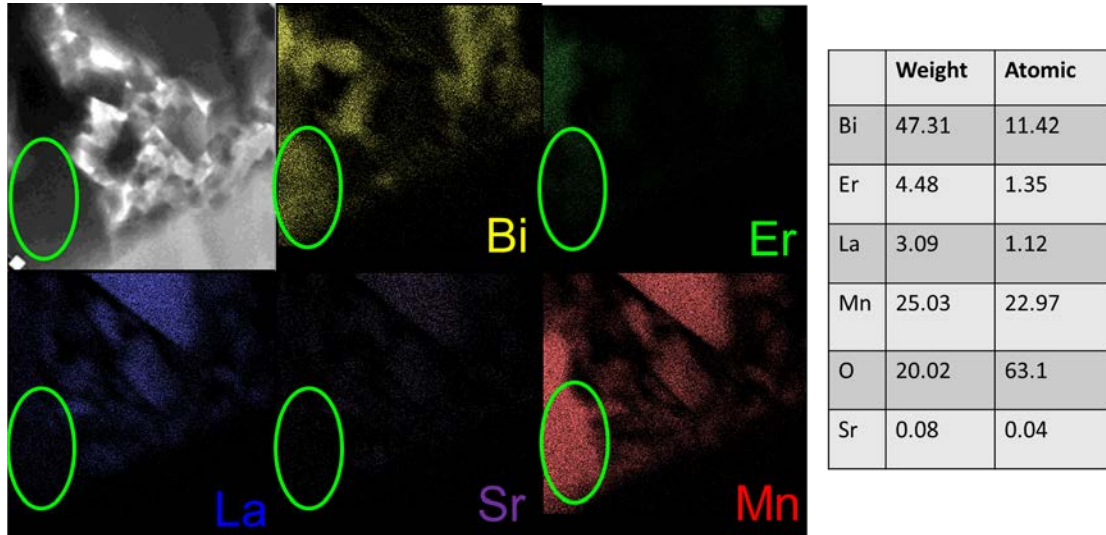


Figure 3.3.8: TEM micrograph and EDS mapping of LSM-ESB cathode aged for 500 h at 650 °C. The green circle indicates a BiMn_2O_5 particle. The table shows the point analysis of the area with a consistent ratio of Bi and Mn.

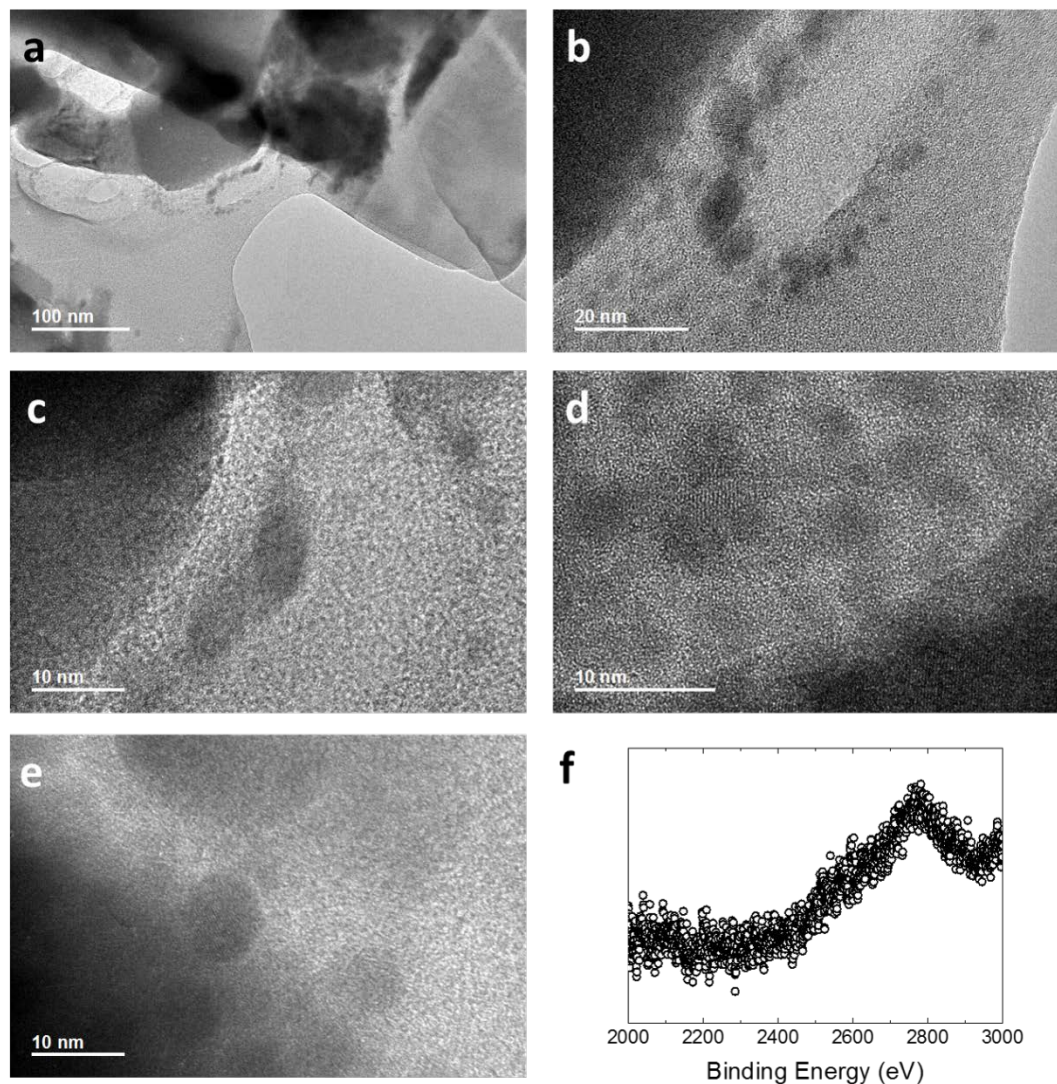


Figure 3.3.9: (a-e) TEM micrographs of bismuth nanoparticles precipitated into porous electrode surface, and (f) EELS binding energy of nanoparticles with M4 and M5 edges 2688 eV and 2580 eV, respectively.

3.4 Conclusion

LSM-ESB symmetric cells were aged at LT-SOFC temperatures in air to determine the long-term durability. Using *in situ* EIS we separated the ohmic and non-ohmic contributions to the cell performance as a function of time. Below 650 °C the anion ordering in ESB plays an important role in limiting the cathode performance. The ordering not only decreases ionic conductivity but also the catalytic properties of the

cathode. In order to leverage the high ionic conductivity of bismuth-oxide in LT-SOFC composite cathodes, anion ordering must be suppressed. At 650 °C, above the order-disorder transition of the ESB, the formation of secondary phases due to reactions between ESB and LSM as well as ESB coarsening are the main degradation mechanisms. The volatility of bismuth at high temperature may be the major reason. These findings reveal the potential degradation mechanisms which must be addressed in order to implement bismuth oxide based LT-SOFCs.

Chapter 4: LSM-ESB Particle Size Optimization

4.1 Introduction

Goals for durability in SOFCs typically call for degradation rates on the order of a few percent per 1000 hours to be economically competitive in the current energy generation market³. Various approaches have been investigated to increase the durability of cathodes including altering the chemical composition of the components, pivoting to different cathode systems, and modifying the processing. An appealing of method reducing cathode degradation is optimizing the cathode microstructure by varying the relative particle size of the composite components. This tactic does not require repeated synthesis of new materials or the introduction of new materials. In the work we investigate degradation rate of LSM-ESB cathodes with different ESB particle sizes.

4.2 Experimental

Two methods were used to produce ESB of varying particle sizes: wet chemical synthesis via reverse-strike co-precipitation and solid-state reaction with ball milling. Reverse-strike coprecipitation is a wet chemical process designed to produce nanometer-sized, compositionally uniform ESB powders⁵. To make the coprecipitated ESB (cpESB), stoichiometric $\text{Bi}(\text{NO}_3)_3 \cdot x\text{H}_2\text{O}$ and $\text{Er}(\text{NO}_3)_3 \cdot 5\text{H}_2\text{O}$ were dissolved in 100 mL of fuming HNO_3 . The mixtures was added drop-wise into 500 mL of NH_4OH . The pH was monitored and NH_4OH was added as needed to maintain the pH below 10. The mixture was vacuum filtered using a 220 nm nitrocellulose filter and rinsed with deionized water. The resulting powder was then calcined at 550 °C for 4 h. The other approach to producing various powder sizes is carefully controlled ball milling. 2 g of

ESB powder produced by solid-state processing (ssESB, Trans-Tech) were combined with 15 mL of ethanol and 100 g of 5 mm YSZ milling media in 60 mL HDPE bottles and milled for 4 h, 21 h, 164 h or 310 h.

A small portion of each resulting powder was reserved for laser scattering, SEM and XRD. The process of making the cathode paste was carefully carried out to limit further particle size modifications. 0.9 g of ESB powder was combined with 0.6 g of LSM powder (60:40 mass ratio) with 15 mL of ethanol and 100 g of 5 mm YSZ milling media in 60 mL HDPE bottles. Each LSM-ESB mixture was milled for 60 minutes before being made into paste by the process in Chapter 2.

Each paste was used to make sets of symmetric cells using methods previously described. To gauge the repeatability of our tests, the cells were aged in the four-cell reactor in sets of two, e.g. two LSM-ESB Milled 4 h and two LSM-ESB Milled 310 h. The samples were heated to 725 °C to sinter the Au contacts and then cooled to 650 °C and aged for 180 h. During aging, 50 ccm of compressed air (zero grade) was flowed through the reactor and EIS was measured hourly.

4.3 Particle Size Analysis

The powder XRD of each ESB sample is shown in Figure 4.3.1A. Among the ssESB samples there is no noticeable change in the ESB phase purity after different milling times. In addition, the reverse-strike coprecipitation achieves pure ESB phase. The broadening of the (200) peak of each ESB sample is shown in Figure 4.3.1.B along with the crystallite size of each sample derived from the Scherrer equation. In general, with increased milling time there is a decrease in crystallite size with cpESB achieving the smallest crystallite size overall.

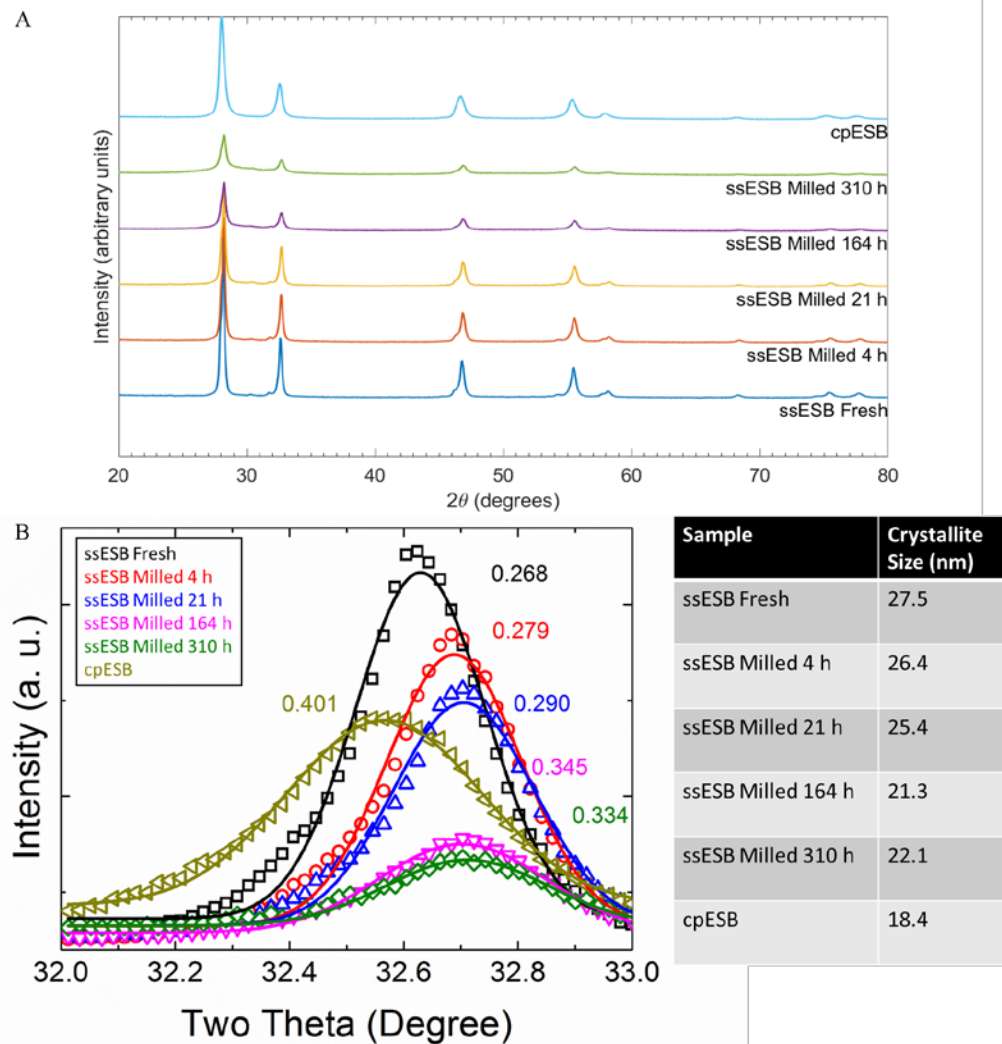


Figure 4.3.1: A) Powder XRD spectra of cpESB and ssESB milled for various durations. B) Close up of (200) ESB peak with full width at half maximum values and table of crystallite size calculated from the Scherrer equation.

The SEM micrographs of the ESB samples are shown in Figure 4.3.2. With increased milling time there is a general trend of decreased particle size. There is a particularly noticeable change in the size between 21 h and 164 h of milling. However, the ssESB milled 164 h, ssESB milled 310 h and cpESB show little change.

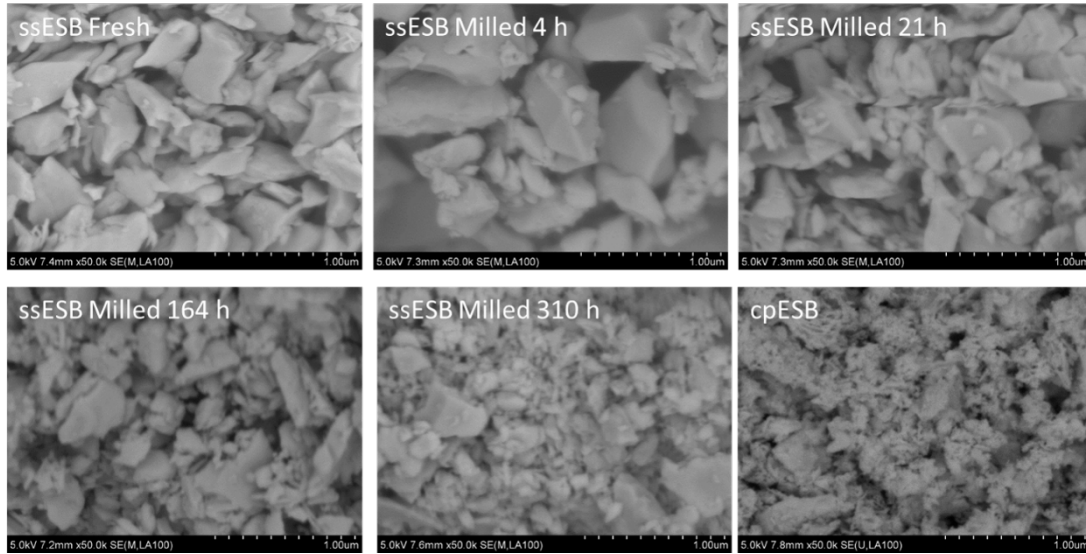


Figure 4.3.2: SEM micrographs of cpESB powder and ssESB powders milled for various durations.

The particle size distribution collected from laser scattering is shown in Figure 4.3.3 along with the average ESB particle size of each sample. Over all the average particle size ranged from 1.28 μm to 0.087 μm . The first four hours of milling the ssESB had little effect of the average particle size. The ssESB milled for 21 h shows the broadest size distribution of the samples measured. This milling process seems to be limited to producing particles of about 0.09 μm particles. This limit is reached after at least 164 h, after which there is no further size reduction. At first glance the cpESB seems to have the greatest size at 1.2 μm . However, after consulting the SEM, this is likely attributed to agglomeration from the wet chemical process. To estimate the particle size within the agglomerate, a small portion of cpESB was ball milled for one hour before calcining to break apart the agglomerate before the calcining process cemented the particles together. Laser scattering of these particles indicated that the aggregate was formed of particles roughly a magnitude smaller in diameter.

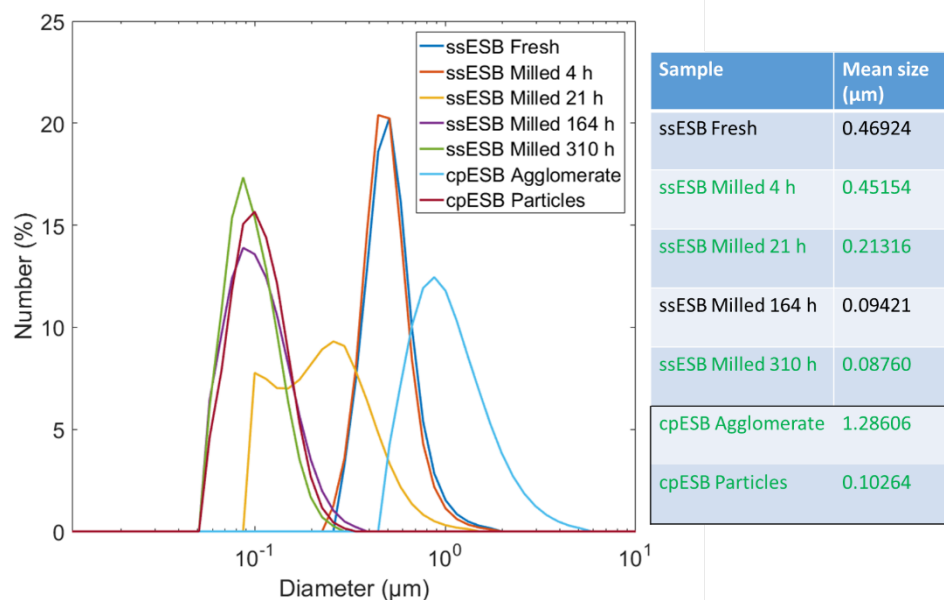


Figure 4.3.3: Laser scattering of cpESB powder and ssESB powders milled for various durations. Ethanol was used to disperse the particles. The table shows the average particle size of each sample. The samples highlighted in green were made into cathode paste.

4.4 Electrochemical Analysis

Figure 4.4.1 shows the Nyquist plots of one of each sample during aging. Each sample shows the aging primarily in the low-frequency arc with little to no change in the high frequency. This is particularly apparent in the ssESB milled for 310 h when the low-frequency arc nearly doubles in size.

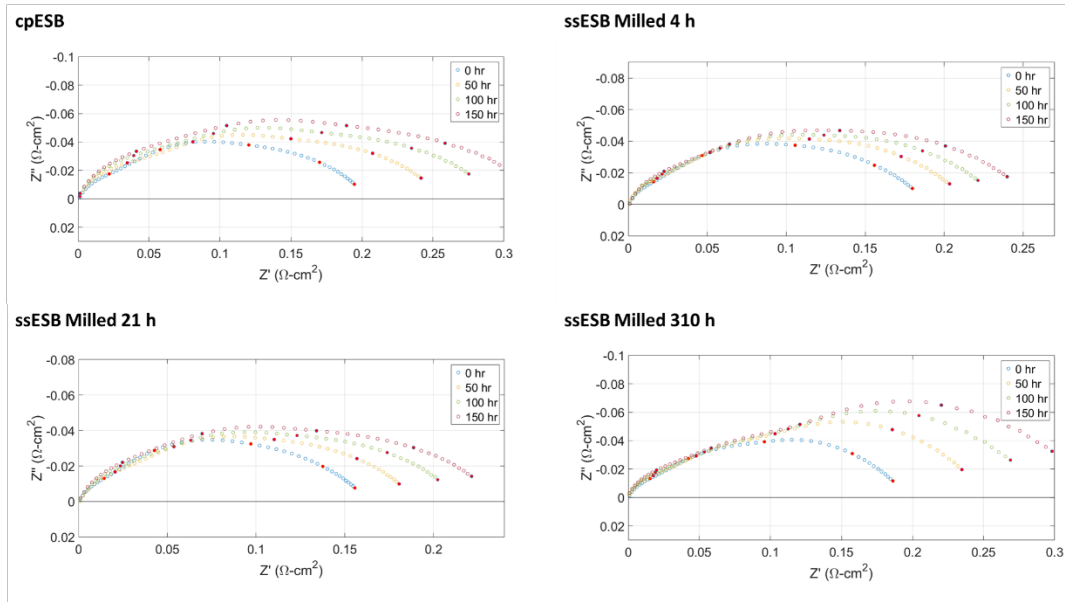


Figure 4.4.1: Nyquist plots of LSM-ESB symmetric cells aged at 650 °C. cpESB, ssESB milled for 4 h, 21 h and 310 h were used for the LSM-ESB composite cathode. The plots are shown for 0 h, 50 h, 100 h, and 150 h.

The non-ohmic and ohmic contributions extracted from the EIS are shown in Figure 4.4.2. A and Figure 4.4.2. B, respectively. Little to no degradation is seen in any of the samples' ohmic conductivity. This is consistent with the previous work and is expected since the ESB electrolyte, the main contribution to the ohmic conductivity, is the same for each sample. Though there is no difference in performance of the small particle size ESB, the 4 h milled ssESB has dramatically lower ohmic conductivity. It is unclear as to why this is the case though it may be attributed to poorer contact between the electrolyte and cathode layers.

Initially, the 4 h, 310h milled ssESB, and cpESB have similar ASR. The ssESB milled for 21 h, on the other hand, begins with significantly lower non-ohmic ASR. One possible explanation for this is the wide particle size distribution of the ESB. As the varied particles sinter they may pack more densely extending the effective TPB.

Each sample was fitted with a linear trend line, though the small ESB samples, 310 h milled ssESB and cpESB, displayed some curvature in the degradation rate.

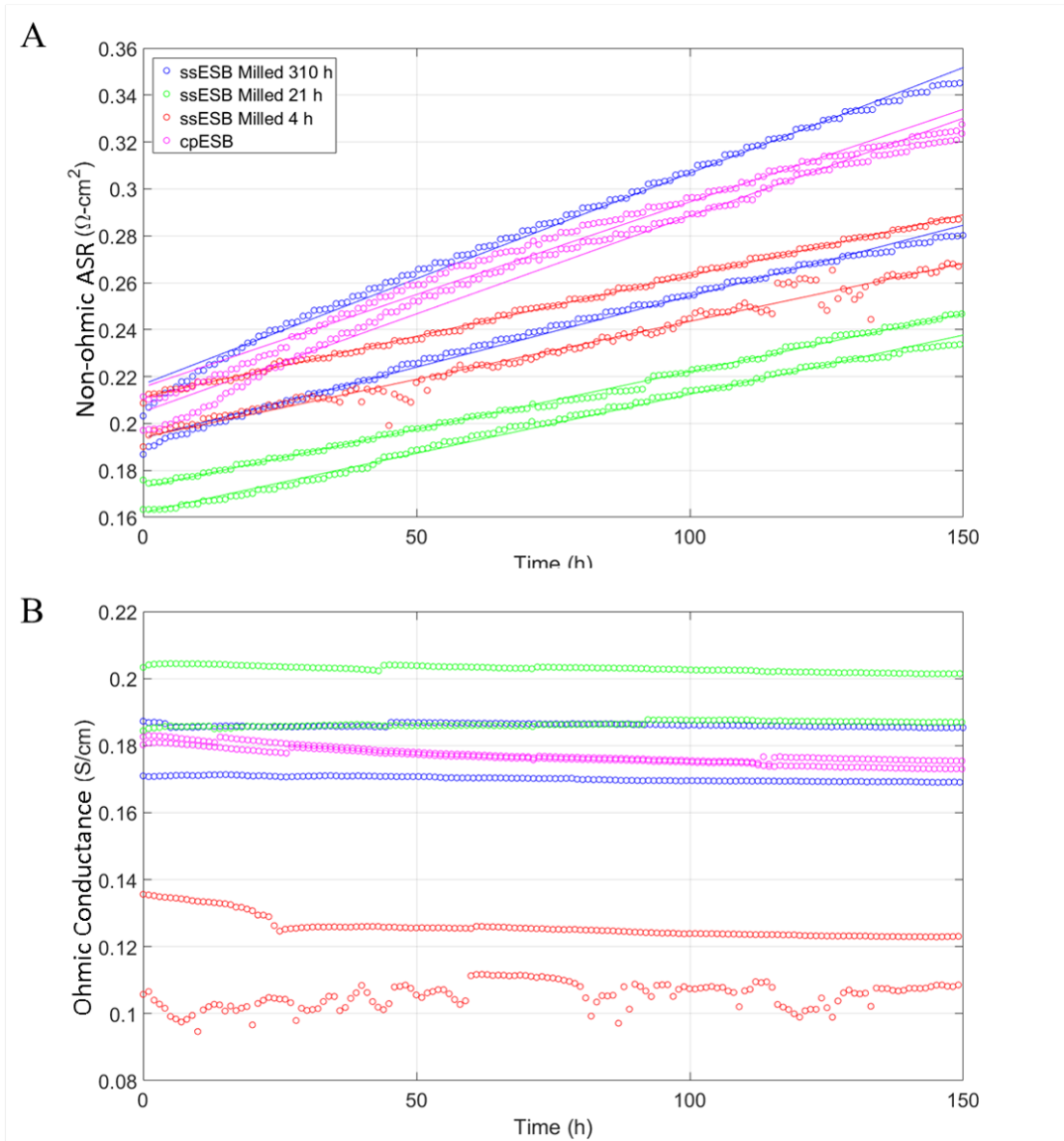


Figure 4.4.2: A) Non-ohmic ASR of LSM-ESB symmetric cells aged at 650 °C fitted with linear trend lines. B) Time dependence of ohmic contribution of LSM-ESB symmetric cells aged at 650 °C.

To account for variability in the initial performance, the degradation rate was normalized to the starting non-ohmic ASR of each sample. The degradation rates in %/100h are plotted against r , the ESB:LSM particle size ratio in Figure 4.4.3. In

general, the degradation rate decreases with the particle size ratio. Since grain coarsening and phase formation both increase with surface area, it follows that smaller particles would degrade more quickly than larger particles. In the absence of more data, the model for fitting the trend is unclear. An exponential fit is shown as a possible fit for describing the data. Another conclusion drawn from the data is that the manufacturing processes, reverse-strike coprecipitation and solid-state milling, yield comparable performance with similar particle sizes.

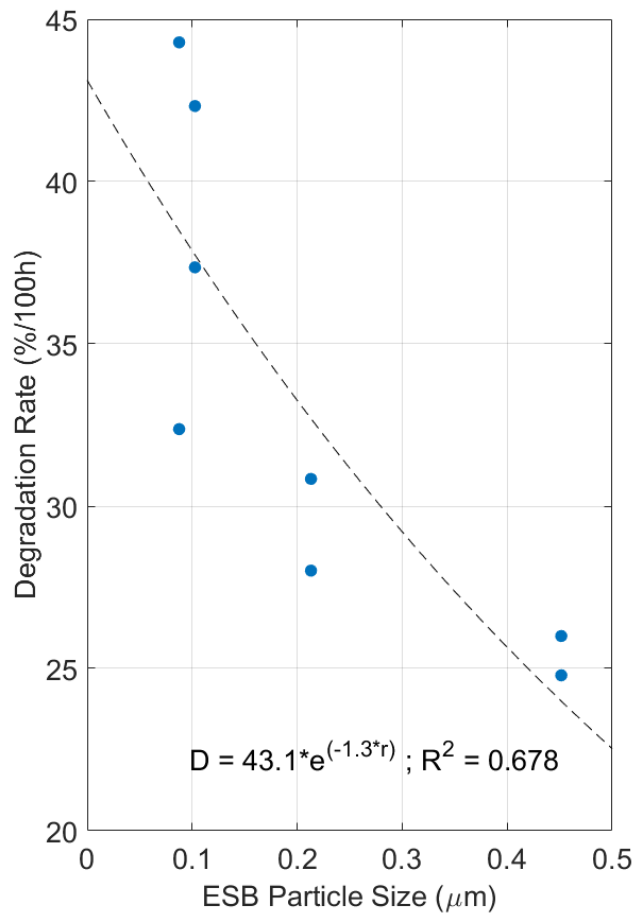


Figure 4.4.3: Degradation rate of non-ohmic ASR plotted against the ESB particle size. Dashed line show a potential exponential fit of data.

If the increased durability of the large ESB particles is due to a resistance in secondary phase formation, this should be apparent in the phase analysis. The XRD of each of the aged cathodes is shown in Figure 4.4.4. As anticipated, the ssESB milled for 4 h shows almost no secondary phase formation after aging. Interestingly, the 21 h sample shows almost identical phase formation as the 310 h sample. This may, again, be due to the wide particle size distribution of the 21 h sample.

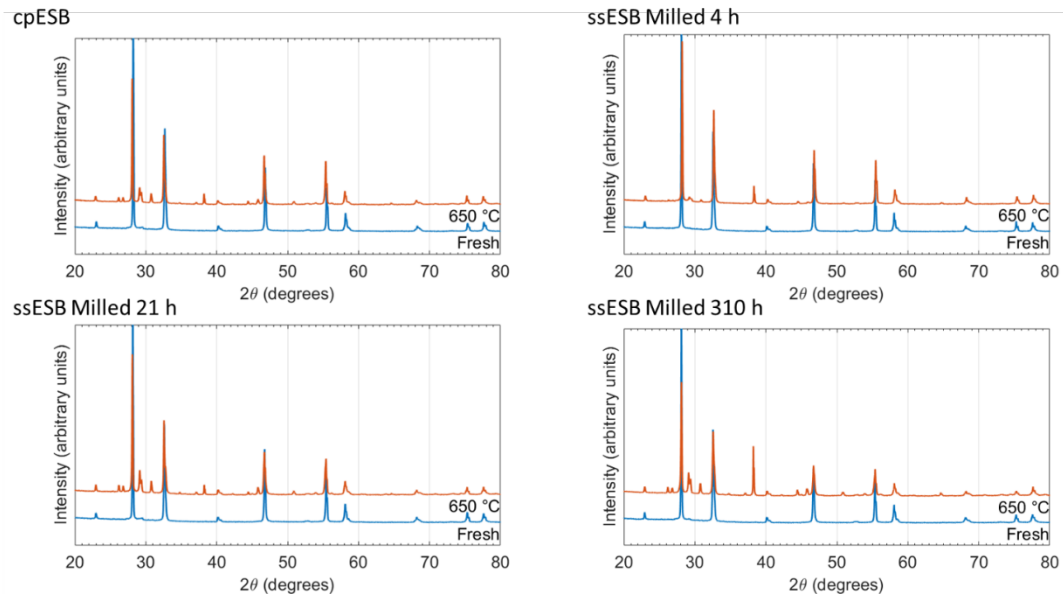


Figure 4.4.4: XRD spectra of freshly sintered LSM-ESB symmetric cells and LSM-ESB cells aged for 180 h at 650 °C. cpESB, ssESB milled for 4 h, 21 h and 310 h were used for the LSM-ESB composite cathode.

4.5 Conclusion

Various ESB particle sizes were prepared using two different methods: reverse-strike coprecipitation and solid-state ball milling. The particle size of the ESB powders was quantified using laser scattering, SEM, and XRD. The LSM-ESB powders were incorporated into cathode paste for symmetric cells and aged at 650 °C for 180 h. The ohmic conductivity extracted from EIS showed little difference in the smaller particle sizes but lower performance in the ssESB milled for 4 h. The largest and smallest

particles had similar non-ohmic ASRs. However, the middle sample, ssESB milled for 21 h, had a lower initial ASR. An analysis of the degradation rates found that larger particle size ratios yielded improved the durability, possibly due to the decrease of active sites for chemical reactions.

Chapter 5: Future Work

5.1 Long-Term Aging

- *In-situ* EIS is useful in characterizing the durability of SOFC cathodes and can be used to analyze the performance and durability of composite cathodes with alternative lanthanide doped or double-doped bismuth oxides such as $\text{Dy}_{0.08}\text{W}_{0.04}\text{Bi}_{0.88}\text{O}_{1.56}$ (DWSB)⁴⁴.
- Further characterization of the microstructure is useful to quantitatively determine the degree of grain coarsening as well as measure TPB length and delamination.
- Contaminants, such as chromium from interconnects, CO_2 , and H_2O , have been shown to reduce performance and increase degradation in other cathodes. The effects of these contaminants should be evaluated on LSM-ESB.

5.2 Particle Size Analysis

- A trend between the LSM-ESB particle size ratio and degradation rate was found for a narrow window of size ratios. A wider range of particle ratios should be considered to find the limits of this trend. In addition, the impact of LSM particle size should also be investigated.
- An overall ratio of 60:40 ESB:LSM by mass was used for all of the particle size optimization study. Adjustments in the overall mass ratio may be necessary to compensate for changes in performance due to the difference in particle size ratio.

Bibliography

1. Wachsman, E. D. & Lee, K. T. Lowering the Temperature of Solid Oxide Fuel Cells. *Science* (80-.). **334**, 935–939 (2011).
2. EG&G Technical Services, I. Fuel Cell Handbook. *Fuel Cell 7 Edition*, 1–352 (2004).
3. National Renewable Energy Laboratory. 1-10 kW Stationary Combined Heat and Power Systems Status and Technical Potential. (2010).
4. Lee, K. T., Lidie, A. a., Yoon, H. S. & Wachsman, E. D. Rational Design of Lower-Temperature Solid Oxide Fuel Cell Cathodes via Nanotailoring of Co-Assembled Composite Structures. *Angew. Chemie Int. Ed.* **53**, 13463–13467 (2014).
5. Lee, K. T. *et al.* Highly functional nano-scale stabilized bismuth oxides via reverse strike co-precipitation for solid oxide fuel cells. *J. Mater. Chem. A* **1**, 6199–6207 (2013).
6. Energy, U. S. D. of. Types of Fuel Cells. *Website*
7. Murray, E. P., Tsai, T. & Barnett, S. a. A direct-methane fuel cell with a ceria-based anode. *Nature* **400**, 649–651 (1999).
8. Lee, K. T., Yoon, H. S. & Wachsman, E. D. The evolution of low temperature solid oxide fuel cells. *J. Mater. Res.* **27**, 2063–2078 (2012).
9. Jabbar, M. H. A. Anodes for solid oxide fuel cells operating at low temperatures. (2012).
10. Hagen, a., Liu, Y. L., Barfod, R. & Hendriksen, P. V. Assessment of the Cathode Contribution to the Degradation of Anode-Supported Solid Oxide Fuel Cells. *J. Electrochem. Soc.* **155**, B1047 (2008).

11. Adler, S. B. Factors governing oxygen reduction in solid oxide fuel cell cathodes. *Chem. Rev.* **104**, 4791–4843 (2004).
12. Eguchi, K., Setoguchi, T., Inoue, T. & Arai, H. Electrical properties of ceria-based oxides and their application to solid oxide fuel cells. *Solid State Ionics* **52**, 165–172 (1992).
13. Takahashi, T., Esaka, T. & Iwahara, H. Conduction in Bi₂O₃-based oxide ion conductors under low oxygen pressure . I . Current blackening of the Bi₂O₃-Y₂O₃ electrolyte. *J. Appl. Electrochem.* **7**, 299–302 (1977).
14. Park, J. Y., Yoon, H. & Wachsman, E. D. Fabrication and characterization of high-conductivity bilayer electrolytes for intermediate-temperature solid oxide fuel cells. *J. Am. Ceram. Soc.* **88**, 2402–2408 (2005).
15. Park, J. Y. & Wachsman, E. D. Stable and high conductivity ceria/bismuth oxide bilayer electrolytes for lower temperature solid oxide fuel cells. *Ionics (Kiel)*. **12**, 15–20 (2006).
16. Shuk, P., Wiemhöfer, H.-D., Guth, U. & Göpel, W. New solid electrolytes based on bismuth oxide. *Ionics (Kiel)*. **2**, 46–52 (1996).
17. Shuk, P. Oxide ion conducting solid electrolytes based on Bi₂O₃. *Solid State Ionics* **89**, 179–196 (1996).
18. Jiang, N. & Wachsman, E. D. Structural Stability and Conductivity of Phase-Stabilized Cubic Bismuth Oxides. *J. Am. Ceram. Soc.* **82**, 3057–3064 (1999).
19. Sammes, N. M., Tompsett, G. A., Nafe, H. & Aldinger, F. Bismuth Based Oxide Electrolytes- Structure and Ionic Conductivity. *J. Eur. Ceram. Soc.* **19**, 1801–1826 (1999).

20. Boyapati, S., Wachsman, E. D. & Chakoumakos, B. C. Neutron diffraction study of occupancy and positional order of oxygen ions in phase stabilized cubic bismuth oxides. *Solid State Ionics* **138**, 293–304 (2001).
21. Verkerk, M. J. & Burggraaf, A. J. High Oxygen Ion Conduction in Sintered Oxides of the Bi₂O₃-Ln₂O₃ System. *Solid State Ionics* **3/4**, 463–467 (1981).
22. Aidhy, D. S., Sinnott, S. B., Wachsman, E. D., Phillpot, S. R. & Nino, J. C. Structure of d-Bi₂O₃ from density functional theory: A systematic crystallographic analysis. *J. Solid State Chem.* **182**, 1222–1228 (2009).
23. Wachsman, E. D., Boyapati, S., Kaufman, M. J. & Jiang, N. Modeling of Ordered Structures of Phase-Stabilized Cubic Bismuth Oxides. *J. Am. Ceram. Soc.* **83**, 1964–1968 (2000).
24. Boyapati, S., Wachsman, E. D. & Jiang, N. Effect of oxygen sublattice ordering on interstitial transport mechanism and conductivity activation energies in phase-stabilized cubic bismuth oxides. *Solid State Ionics* **140**, 149–160 (2001).
25. Jiang, N. *et al.* Anion ordering in aged stabilized bismuth oxide. *Mater. Lett.* **22**, 215–219 (1995).
26. Mahato, N., Banerjee, A., Gupta, A., Omar, S. & Balani, K. Progress in material selection for solid oxide fuel cell technology: A review. *Prog. Mater. Sci.* **72**, 141–337 (2015).
27. Ding, D. *et al.* Efficient electro-catalysts for enhancing surface activity and stability of SOFC cathodes. *Adv. Energy Mater.* **3**, 1149–1154 (2013).
28. Ormerod, M. R. Solid oxide fuel cells. *Chem. Soc. Rev.* **32**, 17–28 (2003).

29. Nielsen, J., Hjalmarsson, P., Hansen, M. H. & Blennow, P. Effect of low temperature in-situ sintering on the impedance and the performance of intermediate temperature solid oxide fuel cell cathodes. *J. Power Sources* **245**, 418–428 (2014).
30. Lee, K. T. *et al.* Interfacial modification of $\text{La}_{0.80}\text{Sr}_{0.20}\text{MnO}_{3-\delta}$ - $\text{Er}_{0.4}\text{Bi}_{0.6}\text{O}_3$ cathodes for high performance lower temperature solid oxide fuel cells. *J. Power Sources* **220**, 324–330 (2012).
31. Xiong, C. *et al.* Long-Term Cr Poisoning Effect on LSCF-GDC Composite Cathodes Sintered at Different Temperatures. *J. Electrochem. Soc.* **163**, F1091–F1099 (2016).
32. Oh, D., Gostovic, D. & Wachsman, E. D. Mechanism of $\text{La}_{0.6}\text{Sr}_{0.4}\text{Co}_{0.2}\text{Fe}_{0.8}\text{O}_3$ cathode degradation. *J. Mater. Res.* **27**, 1992–1999 (2012).
33. Liu, Y. L., Thyrn, K., Chen, M. & Hagen, A. Microstructure degradation of LSM-YSZ cathode in SOFCs operated at various conditions. *Solid State Ionics* **206**, 97–103 (2012).
34. Liu, Y. L. *et al.* Microstructural studies on degradation of interface between LSM-YSZ cathode and YSZ electrolyte in SOFCs. *Solid State Ionics* **180**, 1298–1304 (2009).
35. Sato, K., Kinoshita, T. & Abe, H. Performance and durability of nanostructured $(\text{La}_{0.85}\text{Sr}_{0.15})_{0.98}\text{MnO}_3$ /yttria-stabilized zirconia cathodes for intermediate-temperature solid oxide fuel cells. *J. Power Sources* **195**, 4114–4118 (2010).

36. Irvine, J. T. S., Sinclair, D. C. & West, A. R. Electroceramics: characterization by impedance spectroscopy. *Adv. Mater.* **2**, 132–138 (1990).
37. Boukamp, B. A. A Linear Kronig-Kramers Transform Test for Immittance Data Validation. *J. Electrochem. Soc.* **142**, 1885–1894 (1995).
38. Agarwal, P., Orazem, M. E. & Garcia-Rubio, L. H. Measurement Models for Electrochemical Impedance Spectroscopy. *J. Electrochem. Soc.* **139**, 1917–1927 (1992).
39. Kharton, V. V., Naumovich, E. N., Yaremchenko, A. A. & Marques, F. M. B. Research on the electrochemistry of oxygen ion conductors in the former Soviet Union - IV. Bismuth oxide-based ceramics. *J. Solid State Electrochem.* **5**, 160–187 (2001).
40. Kharton, V., Naumovich, E. & Samokhval, V. Formation and properties of reaction layers of cobaltite electrodes on bismuth oxide electrolytes. *Solid State Ionics* **99**, 269–280 (1997).
41. Jaiswal, A., Hu, C.-T. & Wachsman, E. D. Bismuth Ruthenate-Stabilized Bismuth Oxide Composite Cathodes for IT-SOFC. *J. Electrochem. Soc.* **154**, B1088 (2007).
42. Wachsman, E. D., Ball, G. R., Jiang, N. & Stevenson, D. A. Structural and defect studies in solid oxide electrolytes. *Solid State Ionics* **52**, 213–218 (1992).
43. Marschman, S. C. & Lynch, D. C. Review of the Bi and Bi-O Vapor Systems. *Can. J. Chem. Eng.* **62**, 875–879 (1984).
44. Jiang, N., Wachsman, E. D. & Jung, S. H. A higher conductivity Bi₂O₃-based

electrolyte. *Solid State Ionics* **150**, 347–353 (2002).